

Electronic and Vibrational Coherence in the Core Light-Harvesting Antenna of *Rhodopseudomonas viridis*

Vladimir Novoderezhkin,[†] René Monshouwer,[‡] and Rienk van Grondelle^{*,‡}

A. N. Belozersky Institute of Physico-Chemical Biology, Moscow State University, Moscow 119899, Russia, and Department of Biophysics, Faculty of Sciences, Vrije Universiteit, De Boelelaan 1081, 1081 HV Amsterdam, The Netherlands

Received: May 22, 2000; In Final Form: October 4, 2000

In this paper we explain the wavelength-dependent oscillatory features in the pump–probe kinetics of the core LH1 antenna of *Rhodopseudomonas viridis* (Monshouwer, R.; Baltuška, A.; van Mourik, F.; van Grondelle, R. *J. Phys. Chem. A* **1998**, 102, 4360). A quantitative fit of the data was obtained using the doorway–window representation of the nonlinear optical response in the vibrational eigenstate basis. In contrast to LH1/LH2 complexes from the BChl *a*-containing species, the LH1 antenna of *Rps. viridis* is characterized by a strong coupling of the excitonic states with two underdamped low-frequency modes (58 and 110 cm^{−1} at 77 K). Following a short femtosecond excitation pulse, this gives rise to the intense oscillations observed in the pump–probe traces, including their time and excitation/detection wavelength dependence. Furthermore, it leads to a pronounced and specific heterogeneity of the major absorption band due to the combined effects of the exciton splitting, disorder, and the presence of vibrational sidebands. The sharp maxima in the second derivative of the low-temperature absorption spectrum (Monshouwer, R.; Visschers, R. W.; van Mourik, F.; Freiberg, A.; van Grondelle, R. *Biochim. Biophys. Acta* **1995**, 1229, 373) were assigned to the lowest exciton–vibrational transitions. The wavelength dependence of the experimentally observed oscillatory pattern suggests a different vibrational coherence decay for the ground- and excited-state wave packets. This can be explained by assuming the (incoherent) migration of the delocalized exciton (polaron) around the ringlike antenna with a characteristic time constant of 0.9–1.5 ps at 77K.

Introduction

In photosynthesis three fundamental events determine the high quantum yield of the primary processes: (i) absorption of a solar photon and transfer of the electronic excitation in (bacterio)chlorophyll ((B)Chl)–protein aggregates of a light-harvesting antenna, (ii) energy trapping by the special pair P of the reaction center (RC), and (iii) primary charge separation from the excited-state P* of the special pair.^{1–4} In the case of purple bacteria an antenna unit contains a strongly coupled ringlike aggregate of BChls.^{5–8} Energy transfer within such an antenna unit and between neighboring units occurs on subpicosecond and picosecond time scales, respectively.³ The time constant for the trapping of the electronic excitation in the antenna by the special pair of the RC is about 30–80 ps,^{9–11} whereas the charge separation from P* takes place in a few picoseconds.^{12,13}

It is well established that primary energy transfer occurs via singlet molecular excitons. Generally, these excitons are coupled to collective nuclear motions (intramolecular, intermolecular, protein) of the chromophore–protein complexes of the antenna and RCs. In the conventional theory of energy and electron transfer (incoherent Förster theory) these nuclear motions are supposed to be thermally equilibrated. This seems to be reasonable for the relatively slow antenna–RC transfer, but this may not be the case for the fast energy transfer in antenna and charge transfer in RCs. An adequate physical model for the

excitation and electron transfer dynamics in the (sub)picosecond time domain should include the effects of long-lived vibrational coherences, which have frequently been observed first in bacterial RCs,^{14–21} later in bacterial antennas,^{22–29} chlorosomes,^{30,31} and recently in the major plant light-harvesting complex LHCII.³²

In photosynthetic purple bacteria, a light-harvesting antennae generally consist of a peripheral antenna (LH2) and a core antenna complex (LH1); the latter directly surrounds the reaction centers. The elementary subunit of these complexes consists of a pair of transmembrane polypeptides, α and β , binding two or three bacteriochlorophyll (BChl) molecules.³³

A high-resolution three-dimensional X-ray structure of the peripheral LH2 antenna was obtained for the purple bacteria *Rhodopseudomonas (Rps.) acidophila*⁵ and *Rhodospirillum (Rs.) molischanum*.⁷ It was discovered that these antenna complexes consist of $\alpha\beta$ pigment–protein subunits arranged in a high-symmetry ringlike structure. The LH2 antenna from *Rps. acidophila* contains 9 $\alpha\beta$ subunits, with each subunit binding two BChl850 molecules and one BChl800 molecule. Analysis of the pigment arrangement has shown that the 18 BChl850 molecules form a C₉-symmetric ring with a dimeric unit cell, whereas the 9 BChl800 molecules form a C₉-symmetric ring with a monomeric unit cell in a plane that is vertically displaced and parallel to the B850 ring. The results of ab initio molecular orbital calculations showed the strong coupling between the BChl850 and weak coupling between the BChl800 molecules.^{8,34,35} The structure of the LH2 antenna of *Rs. molischanum* is similar to that of *Rps. acidophila*, but this antenna

* To whom correspondence should be addressed. E-mail: rienk@nat.vu.nl. Fax: +31-20-4447899.

[†]Moscow State University.

[‡]Vrije Universiteit.

TABLE 1: Parameters of the Vibrational Modes Coupled to Electronic Excitations in the LH1 and LH2 Complexes of Purple Bacteria^a

species	T, K	pump/probe, fs	main (minor) freq, cm ⁻¹	damping const γ^{-1} , fs	ref
<i>Rb. sphaeroides</i> LH1	4	40/40	(20), (90), 110, (180), (300)	200–400	22
	300	40/40	110	300	22
	300	FL	105	450	25
	300	TG	100, 190	500	27
	300	3PE	110*, 190#, (560), (750)	700*, 400#	27
<i>Rb. sphaeroides</i> LH2	4	40/40	90, 135		23
	300	TG	(27), 98*, 162#, (185), (432)	390*, 320#	26
	300	3PE	110*, 190#, (750), (920)	700*, 400#	27
<i>Rs. rubrum</i> LH1	77	40/40	65, 110, (150), (175)		23
<i>Rs. rubrum</i> B820 subunit	300	35/35	(20), (50), 115, 175		28
BChl <i>a</i> in solution	4	86/86	(104)		23
	300	86/86	-		23
<i>Rps. viridis</i> LH1	4	100/100	(40), 67*, 104#, (130)	850*, 660#	29
	77	100/100	(28), 65*, 103#, (133), (180)	680*, 670#	29
	300	100/100	48*, 108#, (160), (190)	720*, 470#	29

^a The data was obtained by pump–probe, fluorescence upconversion (FL), transient grating (TG), and three-pulse echo peak shift (3PE) measurements. The damping constants γ^{-1} correspond to the main oscillatory components. The components with different decay times (and the corresponding damping constants) are distinguished by superscripts (*, #).

complex consists of 8 $\alpha\beta$ subunits and the pigment–protein complex exhibits C_8 symmetry.

No high-resolution structure is available for the LH1 antenna, but analysis of 2D crystals of reconstituted LH1 from *Rhodospirillum* (*Rs.*) *rubrum* suggested that the core antenna is also arranged in a ring which consists of 16 $\alpha\beta$ subunits with each subunit binding two BChl875 molecules.⁶ In vivo in the presence of the puf-X protein the ring is probably opened^{36–39} and the RC-LH1 core is arranged in a highly ordered structure.^{38,39}

Coherent vibrational dynamics in the LH1 and LH2 antennae were studied by femtosecond pump–probe,^{22–24,28,29} fluorescence upconversion,²⁵ transient gratings,^{26,27} and photon-echo spectroscopies.²⁷ The results are summarized in Table 1.

One-color 40 fs pump–probe studies of the LH1 and LH2 antennae of *Rb. sphaeroides* were performed at different temperatures and the pump–probe traces revealed strong oscillatory features.^{22,23} For the core antenna (LH1) at 4 K the Fourier transform (FT) spectrum of the pump–probe kinetics revealed a prominent 110 cm⁻¹ mode and minor components at 20, 90, 180, and 300 cm⁻¹. For higher temperatures the amplitude of oscillations decreased, but the 110 cm⁻¹ mode remained observable even at room temperature. The damping time is $\gamma^{-1} \sim 300$ fs at all temperatures. For the peripheral antenna (LH2) the amplitude of oscillations is much smaller as compared with LH1. The FT spectrum revealed two dominant frequencies with comparable amplitudes at 90 and 135 cm⁻¹.

Comparison of the FT of oscillations for the LH1 antenna of *Rb. sphaeroides* and *Rs. rubrum* at 77 K showed the same 110 cm⁻¹ mode for both species.²³ The FT spectrum for *Rs. rubrum* contains an additional pronounced component at 65 cm⁻¹, the corresponding kinetics are essentially nonsinusoidal due to beats between the 65 and 110 cm⁻¹ modes.

Two-color 50 fs pump–probe studies of the LH1 antenna of *Rb. sphaeroides* and *Rs. rubrum* at 77 K were performed in ref 24 with the excitation wavelength at the blue side of the major absorption band. Near the zero-crossing point of the difference absorption spectrum the phase of the oscillations becomes inverted (quickly changed by π). Furthermore, the phase gradually shifts upon tuning the detection wavelength within the ESA and PB/SE regions, but the values of these shifts are relatively small and do not exceed 0.15–0.3 π . The data were qualitatively explained by calculating the pump–probe response of a model three-level system consisting of the ground state, single one-exciton state, and single two-exciton state coupled to one vibrational mode (104 cm⁻¹). The potential surfaces of the three electronic states have their minima at $\Delta^{(0)}$, $\Delta^{(1)}$, and $\Delta^{(2)}$, where Δ is a dimensionless nuclear coordinate. The vibrational dynamics was described by Redfield theory. The third-order response was obtained by expanding the Liouville equation and using a δ -pulse limit for the pump, thus eliminating the ground state wave packet dynamics. It was shown that the shape of oscillations is strongly dependent on the relative displacement of the two-exciton state with respect to the one-exciton state, $\Delta^{(2)} - \Delta^{(1)}$. It was then concluded that this relative displacement should be (within the limits of the model) of opposite sign to the one-exciton state displacement, i.e., $\Delta^{(2)} - \Delta^{(1)} = -(\Delta^{(1)} - \Delta^{(0)})$.

A fluorescence upconversion study (with a 50 fs resolution) of the LH1 antenna of *Rb. sphaeroides* at room temperature²⁵ showed marked oscillations with the frequency of 105 cm⁻¹ and damping constant of 450 fs. Thus, the vibrational dephasing is slower than the exciton relaxation/hopping. The latter manifests itself through the anisotropy decay, which is biphasic, but dominated by the fast 100–110 fs component according to fluorescence upconversion²⁵ and pump–probe studies.^{40–42} A transient grating and three-pulse echo peak shift measurements of isolated LH1 and LH2 complexes of *Rb. sphaeroides* revealed 100–110 and 190 cm⁻¹ oscillations with damping times of 300–700 fs^{26,27} in close agreement with the pump–probe and fluorescence data (see Table 1).

The frequencies of the isotropic pump–probe oscillations observed for the B820 dimeric subunit of the LH1 antenna are the same as for the whole antenna,²⁸ whereas the frequency of the anisotropy oscillations was found to be in the range 450–600 cm⁻¹, reflecting the exciton splitting $2M$ in the B820 dimer. Note that the exciton coupling M in the B820 subunit was estimated to be 230–300 cm⁻¹ from fluorescence polarization,⁴³ singlet–triplet,⁴⁴ and difference absorption studies.⁴⁵

Note that vibrational coherences were not observed for BChl monomers in solution at room temperature.⁴⁶ Only very weak pump–probe oscillations were observed at 4 K in BChl *a* monomers²³ with the frequency of 104 cm⁻¹. This suggests that strong vibrations observed in the LH1, LH2 antennae and B820 subunit originate from intermolecular pigment–pigment modes.

Two-color pump–probe studies of the core antenna (LH1) of *Rps. viridis* have shown that electronic excitations are strongly coupled to two vibrational modes with the frequencies (depending on temperature) of 48–65 and 103–108 cm⁻¹.²⁹ Although the pulses are relatively long in this experiment (100 fs), the amplitude of oscillatory features in pump–probe kinetics is larger than for other LH1 antennae. The surprisingly large damping constant of these oscillations (600–800 fs) significantly exceeds the time of exciton relaxation or hopping as revealed by the ultrafast red shift of the difference absorption (with a time constant of about 130 fs) accompanied by an anisotropy decay (time constant of 150 fs). Upon short-wavelength excita-

tion there are two points where the phase of the oscillations is inverted: near the zero-crossing point and between the PB and SE regions of the difference absorption. The phase shift between these inversion points is much less pronounced than for LH1 of *Rb. sphaeroides* and *Rs. rubrum* using similar excitation conditions.²⁴

In a preceding paper we have proposed a disordered exciton model for the LH1 antenna of *Rps. viridis* which allowed us to explain the shapes of linear and difference absorption.⁴⁷ Here we generalize this model by taking into account the strong coupling of electronic excitations with the two vibrational modes which are, in turn, weakly coupled to the thermal bath. This allowed us to quantitatively explain the evolution of the pump–probe spectrum with time including the strong oscillatory features in the pump–probe kinetics²⁹ as well as the fine structure in the low-temperature absorption spectrum observed for the LH1 antenna of *Rps. viridis*.⁴⁸

Model

The System Hamiltonian. As a model of the light-harvesting antenna we consider an aggregate made out of N two-level molecules interacting with the nuclear degrees of freedom. An electronic state of the system is described by the diagonal and off-diagonal energies, E_n and M_{nm} , corresponding to the intramolecular transition energies and intermolecular couplings. Interactions with fast nuclear modes are described through the dependence of E_n and M_{nm} on collective nuclear coordinates ξ . Interactions with slow nuclear motions can be modeled as diagonal and off-diagonal static disorder (i.e., random shift of the E_n and M_{nm} values). To obtain the third-order optical response, we should consider the one- and two-exciton eigenstates together with the ground state of the aggregate. These exciton states are coupled to new collective coordinates ξ' . The collective nuclear coordinates in the site and exciton representation, ξ and ξ' , are connected via a linear transformation.⁴⁹

To obtain a reduced description in terms of the relevant nuclear coordinates, one can suppose that the exciton states are coupled to a few primary oscillators Q which in turn are coupled to a set of secondary oscillators ξ'' representing the bath.^{50–52} A transformation from the ξ' to (Q, ξ'') coordinates is not unique, so that the choice of the primary coordinates as well as the number of primary oscillators may be different. A theory of energy transfer and nonlinear spectroscopy was developed^{50,52} assuming strong coupling of the electronic and primary coordinates to the bath.

The analysis is greatly simplified in the weak coupling limit when the bath coordinates ξ'' can be completely eliminated. The reduced description in terms of electronic and primary collective variables can be obtained using the Redfield theory.⁵³ This approach was used to model the charge transfer between two electronic states coupled to a single nuclear mode⁵⁴ and the energy transfer in a heterodimer of three-level molecules with two nuclear coordinates.^{55,56}

We start with the Hamiltonian used in the model of Jean and Fleming.⁵⁴ In the case of N electronic states coupled to several primary oscillators (representing normal nuclear modes of the aggregate) the system Hamiltonian is

$$H = \sum_{n=1}^N \sum_j [E_n + \delta E_n - \Omega_j \Delta_j Q_j] |n\rangle \langle n| + \sum_{n \neq m}^N M_{nm} |n\rangle \langle m| \quad (1)$$

where δE_n denote the random shift of the n th site energy due to static disorder, the j th normal mode is characterized by frequency Ω_j , dimensionless oscillator displacement Δ_j (the

same for each site), and dimensionless nuclear coordinate Q_j measured from the minimum of the ground-state surface. We neglect the off-diagonal static disorder as well as off-diagonal coupling to nuclear coordinates (i.e., slow and fast modulation of the M_{nm} values).

Note that in general the oscillator displacement depends on the site number n reflecting a nonuniform lattice deformation due to polaron effects.^{52,57–59} In the case of moderate coupling one can neglect the effects of polaron formation and consider the lattice deformation as uniform.⁶⁰ In this case the exciton–vibrational Hamiltonian does not depend on the exciton wave-number as in eq 1, but only on the total number of excitations.⁶⁰ Such an approximation is reasonable if the polaron is large enough, for example, when the polaron-induced length is larger than the disorder-induced length of the exciton wave functions.^{61,62}

The system Hamiltonian in the eigenstate representation (with taking into account one- and two-exciton states) can be obtained using eq 1 and the expressions of ref 49. We then have

$$H = \sum_k \sum_j [\epsilon_k - \Omega_j \Delta_j Q_j] |k\rangle \langle k| + \sum_q \sum_j [\epsilon_q - 2 \Omega_j \Delta_j Q_j] |q\rangle \langle q| \quad (2)$$

where k and q denote the one- and two-exciton states, ϵ_k and ϵ_q are the corresponding energies (one- and two-exciton eigenvalues of the free exciton Hamiltonian including the static disorder only). Equation 2 shows that the one-exciton states are represented by a manifold of similar potential surfaces with the same (not dependent on k) displacement Δ_j along the Q_j coordinates (but with different “vertical” position along the energy scale, given by ϵ_k). The structure of the two-exciton manifold is the same, i.e., the displacement along Q_j is the same for each q -state. The value of this displacement is equal to $2\Delta_j$, so that the relative displacement of the two-exciton states with respect to the one-exciton states is the same as that for one-exciton states relative to the ground state.

In a more general description, the displacement can be made site-dependent, for example, due to static disorder, i.e., $\Delta_j \rightarrow \Delta_{j,n}$ in eq 1. In this case we will have $\Delta_j \rightarrow \Delta_{j,k}$ and $2\Delta_j \rightarrow \Delta_{j,q}$ in eq 2; i.e., the vibrational structure becomes dependent on the exciton wavenumber k and q . The case of collective intermolecular modes with the site-dependent displacements is very similar to the case when each molecule interacts with its own local nuclear mode. The latter problem was analyzed by Förster⁶³ for two coupled molecules. It was found that not only the displacements but also the shapes of the potential energy surfaces are different for the two exciton states of a dimer. These differences in shape are dependent on intermolecular coupling M and can be neglected only in the strong coupling limit, i.e., $\Omega \Delta^2 / 4M \ll 1$. (This inequality is satisfied for the LH1 antenna, see below.)

The off-diagonal coupling to nuclear coordinates will give rise to some additional displacements of exciton states (also dependent on k and q). For example, the one-exciton displacements will be $\Delta_{j,k} = \Delta_j (1 + \delta \cos(2\pi k/N))$, where δ is the ratio of the off-diagonal (nearest-neighboring) and diagonal couplings. The dependence on wavenumber k is negligible if we are dealing with a few lowest exciton states ($k = 0, \pm 1, \pm 2$) of a large aggregate ($2\pi/N \ll 1$).

Doorway–Window Picture for Molecular Aggregate. We consider the pump–probe spectra of a molecular aggregate in the case when pump and probe pulses are well separated (pump–probe delay is larger than the pulse duration). Using the doorway–window representation,^{51,64,65} we can express the

difference absorption ΔA as

$$\begin{aligned}\Delta A(\tau, \omega_1, \omega_2) &= \text{PB} + \text{SE} + \text{ESA} \\ \text{PB} &= -\omega_2 \langle W^{gg}(\omega_2) D^{gg}(\tau, \omega_1) \rangle \\ \text{SE} &= -\omega_2 \langle \sum_{k,k'} W^{k'k}(\omega_2) D^{kk'}(\tau, \omega_1) \rangle \\ \text{ESA} &= \omega_2 \langle \sum_{k,k'} \tilde{W}^{k'k}(\omega_2) D^{kk'}(\tau, \omega_1) \rangle\end{aligned}\quad (3)$$

where ω_1 and ω_2 are pump and probe frequencies, τ is the pump–probe delay, g and $k(k')$ denote the ground and one-exciton states, respectively. Angular brackets indicate an average over nuclear degrees of freedom (an average over the static disorder is also implied in eq 3). The difference absorption is a sum of the photobleaching (PB), stimulated emission (SE), and excited state absorption (ESA). In the sequential pump–probe experiment, the pump pulse creates a superposition of electronic and vibrational states in the one-exciton manifold together with the hole in the vibronic sublevels of the ground state. The corresponding doorway amplitudes are $D^{kk'}(0, \omega_1)$ and $D^{gg}(0, \omega_1)$. Their independent evolutions during the pump–probe delay, $D^{kk'}(\tau, \omega_1)$ and $D^{gg}(\tau, \omega_1)$, are determined by the bath-induced exciton and vibrational relaxation. The absorption of a weak probe is determined by the overlap of the doorway and window wave packets (eq 3). The initial doorway amplitudes $D^{kk'}(0, \omega_1)$, $D^{gg}(0, \omega_1)$ and the window amplitudes $W^{k'k}(\omega_2)$, $W^{gg}(\omega_2)$ are given by

$$\begin{aligned}D^{gg}(0, \omega_1) &= \int_{-\infty}^{\infty} dt' \int_0^{\infty} dt_1 E_1(t') E_1(t' - t_1) \times \\ &\quad e^{i\omega_1 t_1} \sum_k e^{iH_g t'} V_{gk} e^{-iH_{gk} t_1} V_{kg} \rho_g e^{iH_g t_1} e^{-iH_g t'} + \text{h.c.} \\ W^{gg}(\omega_2) &= \int_{-\infty}^{\infty} dt \int_0^{\infty} dt_3 E_2(t + t_3) E_2(t) \times \\ &\quad e^{i\omega_2 t_3} \sum_k e^{iH_g t} e^{-iH_{gk} t_3} V_{gk} e^{iH_{gk} t_3} V_{kg} e^{-iH_g t} + \text{h.c.} \\ D^{kk'}(0, \omega_1) &= \int_{-\infty}^{\infty} dt' \int_0^{\infty} dt_1 E_1(t') E_1(t' - t_1) \times \\ &\quad e^{i\omega_1 t_1} e^{iH_{k'} t'} e^{-iH_{k't} t_1} V_{k'g} \rho_g e^{iH_{gk} t_1} V_{gk} e^{-iH_{k'} t'} + \text{h.c.} \\ W^{k'k}(\omega_2) &= \int_{-\infty}^{\infty} dt \int_0^{\infty} dt_3 E_2(t + t_3) E_2(t) \times \\ &\quad e^{i\omega_2 t_3} e^{iH_{k'} t_3} V_{k'g} e^{iH_{gk} t_3} V_{gk} e^{-iH_{k'} t_3} e^{-iH_{k'} t} + \text{h.c.} \\ \tilde{W}^{k'k}(\omega_2) &= \int_{-\infty}^{\infty} dt \int_0^{\infty} dt_3 E_2(t + t_3) E_2(t) \times \\ &\quad e^{i\omega_2 t_3} \sum_q e^{-iH_{k'} t} V_{k'q} e^{-iH_{qk} t_3} V_{qk} e^{iH_{k'} t_3} e^{iH_{k'} t} + \text{h.c.}\end{aligned}\quad (4)$$

where E_1 and E_2 are amplitudes of the electric field of pump and probe pulses (they are taken to be real), ρ_g is the steady-state density matrix, V_{gk} and V_{kq} are the matrix elements of the transition dipole operator, H_g , H_k , and H_q are the Hamiltonians of the ground, one-exciton, and two-exciton states. Notice that ρ_g , V_{gk} , V_{kq} , H_g , H_k , and H_q depend on the nuclear coordinates. The time periods t_1 and t_3 correspond to the electronic coherence periods. During the time periods t and t' we have a nuclear wave packet motion in the ground state or coupled nuclear and exciton wave packet motion in the one-exciton manifold.

Expansion in Vibrational Eigenstates. The doorway–window picture allows to obtain simple solutions in the

following limits: (i) pulses short compared with the wave packet dynamics; (ii) pulses long compared with the electronic dephasing time scale; and (iii) snapshot limit, when both conditions are satisfied.^{51,65} A simple solution which is valid for an arbitrary ratio between the pulse duration and the two time scales can be obtained by assuming a Gaussian pulse shape. In the vibrational eigenstate representation we get

$$\text{PB} = -\omega_2 \sum_{c,a} W_{ac}^{gg}(\omega_2) D_{ca}^{gg}(\tau, \omega_1)$$

$$\text{SE} + \text{ESA} = -\omega_2 \sum_{b,d} \sum_{k,k'} \{W_{db}^{k'k}(\omega_2) - \tilde{W}_{db}^{k'k}(\omega_2)\} \cdot D_{bd}^{kk'}(\tau, \omega_1) \quad (5)$$

where a and c denote the vibronic sublevels of the ground state, b , d , and f stand for vibronic sublevels of the one- and two-exciton states, respectively. Equations 5 contain the amplitudes of the doorway and window wave packets. The absence of the angular brackets in eqs 5 indicates that we have taken the trace over the nuclear variables, but these expressions are still dependent on the specific realization of the static disorder (including disorder in the vibrational parameters). In the case of Gaussian pulses, i.e., $E_{1,2}(t) = (\sqrt{\pi\tau_{1,2}})^{-1/2} \exp(-t^2/2\tau_{1,2}^2)$, the initial doorway amplitudes and the window amplitudes are given by

$$D_{ca}^{gg}(0, \omega_1) = \sum_k \sum_b \mu_{cb}^{gk} \mu_{ba}^{kg} \exp(-(\omega_{ca}^{gg}\tau_1)^2/4) \cdot \{P_a L_1(\omega_b^k - \omega_c^g/2 - \omega_d^g/2) + P_c L_1^*(...)\}$$

$$W_{ac}^{gg}(\omega_2) = \sum_k \sum_b \mu_{ab}^{gk} \mu_{bc}^{kg} \exp(-(\omega_{ca}^{gg}\tau_2)^2/4) \cdot \{L_2(\omega_b^k - \omega_c^g/2 - \omega_d^g/2) + L_2^*(...)\}$$

$$D_{bd}^{kk'}(0, \omega_1) = \sum_a \mu_{ba}^{kg} \mu_{ad}^{gk'} \exp(-(\omega_{bd}^{kk'}\tau_1)^2/4) \cdot \{P_a L_1(-\omega_a^g + \omega_b^k/2 + \omega_d^{k'}/2) + P_a L_1^*(...)\}$$

$$W_{db}^{k'k}(\omega_2) = \sum_a \mu_{da}^{k'g} \mu_{ab}^{gk} \exp(-(\omega_{bd}^{kk'}\tau_2)^2/4) \cdot \{L_2(-\omega_a^g + \omega_b^k/2 + \omega_d^{k'}/2) + L_2^*(...)\}$$

$$\tilde{W}_{db}^{k'k}(\omega_2) = \sum_q \sum_f \mu_{df}^{k'q} \mu_{fb}^{qk} \exp(-(\omega_{bd}^{kk'}\tau_2)^2/4) \cdot \{L_2(\omega_f^q - \omega_b^{k'}/2 - \omega_d^{k'}/2) + L_2^*(...)\}$$

$$\omega_a^g = \omega_a; \quad \omega_b^k = \epsilon_k + \omega_b; \quad \omega_f^q = \epsilon_q + \omega_f$$

$$\omega_{ca}^{gg} \equiv \omega_c^g - \omega_a^g; \quad \omega_{bd}^{kk'} \equiv \omega_b^k - \omega_d^{k'} \quad (6)$$

where ω_a^g , ω_b^k and ω_f^q are the energies of the exciton-vibronic states (g, a), (k, b), and (q, f), μ_{ba}^{kg} and μ_{fb}^{qk} are the matrix elements of the (g, a) \rightarrow (k, b) and (k, b) \rightarrow (q, f) optical transitions. In the Condon approximation $\mu_{ba}^{kg} = d_{kg} \langle b|a \rangle$ and $\mu_{fb}^{qk} = d_{qk} \langle f|b \rangle$, where d_{kg} and d_{qk} are electronic transition dipoles, $\langle b|a \rangle$ and $\langle f|b \rangle$ are the Franck–Condon integrals of the corresponding vibrational wave functions; ω_a , ω_b and ω_f are the vibrational energies. P_a and P_c are the steady-state populations of the vibronic sublevels of the ground state, i.e., (g, a) and (g, c) states. $L^*(...)$ denotes the complex conjugate of L (with the same arguments).

To obtain the above expressions we have assumed that the pump and probe pulses are shorter than the time scale of exciton

and vibrational relaxation. But eqs 6 are valid for any ratio between the pulse duration and the time scale of coherent motion of the vibrational or (and) exciton wave packet during the electronic population period (t and t'). This ratio determines the exponential factor in eqs 6, which shows that the coherence between the exciton–vibrational states is appreciable if the splitting between these levels is less than the spectral width of the pulse, i.e., $(\tau_{1,2})^{-1}$. Equations 6 are also valid for an arbitrary ratio between pulse duration and the time scale of electronic dephasing during the electronic coherence period (t_1 and t_3). The dephasing during this period determines the line-shape functions:

$$L_1(\Delta\omega) = \int_0^\infty dt_1 \exp(-(t_1/2\tau_1)^2 + i(\omega_1 - \Delta\omega)t_1 - \Gamma't_1 - (\Lambda't_1/2)^2)$$

$$L_2(\Delta\omega) = \int_0^\infty dt_3 \exp(-(t_3/2\tau_2)^2 + i(\omega_2 - \Delta\omega)t_3 - \Gamma't_3 - (\Lambda't_3/2)^2) \quad (7)$$

Here Γ' and Λ' are dephasing rates of the corresponding electron–vibrational transition. In our model Γ' and Λ' are phenomenological parameters describing a line broadening due to coupling of the system to the fast and slow bath dynamics, respectively (for more details see ref 51). Such a model is commonly used in nonlinear optics to obtain a line shape of the electronic system coupled to several independent degrees of freedom.⁵¹ Integration of eqs 7 yields

$$L_{1,2}(\Delta\omega) = \pi^{1/2} \tilde{\tau}_{1,2} \operatorname{erfc}'(\tilde{\tau}_{1,2}(\Gamma' - i(\omega_{1,2} - \Delta\omega))); \quad \tilde{\tau}_{1,2} = \sqrt{(\tau_{1,2})^2 + 1/\Lambda'^2} \quad (8)$$

where $\operatorname{erfc}'(x) = \exp(-x^2)(1 - \operatorname{erf}(x))$ is the scaled complementary error function.

When the pulses are long compared with the electronic dephasing, we have a Lorentzian line shape $L_{1,2}(\Delta\omega) = (\Gamma' - i(\omega_{1,2} - \Delta\omega))^{-1}$ with the fwhm of $\Gamma = 2\Gamma'$ if $\Lambda' = 0$ and a Gaussian line shape $L_{1,2}(\Delta\omega) + L_{1,2}^*(\Delta\omega) = 2(\pi^{1/2}/\Lambda') \exp(-(\omega_{1,2} - \Delta\omega)^2/\Lambda'^2)$ with the fwhm of $\Lambda = 2(\ln 2)^{1/2}\Lambda'$ if $\Gamma' = 0$. Everywhere below we will use the fwhm values Γ and Λ .

When the pulses are long compared with the electronic dephasing, but short compared with the vibrational (and excitonic) oscillatory period, the exponential term in eqs 6 equals to unity, the line-shape functions are Lorentzians (if $\Lambda' = 0$), and we recover the well-known snapshot limit.⁵¹

Fast Exciton Equilibration. Let us consider the case when the vibrational relaxation is significantly slower than the exciton relaxation. At time delays larger than the exciton equilibration time eqs 5 take the form

$$\begin{aligned} \text{PB} &= -\omega_2 \sum_{c,a} W_{ac}^{gg} \rho_{ca}(\tau) \\ \text{SE} + \text{ESA} &= -\omega_2 \sum_{b,d} \sum_k P_k \{ W_{db}^{kk} - \tilde{W}_{db}^{kk} \} \cdot \rho_{bd}(\tau) \\ \rho_{ca}(0) &= D_{ca}^{gg}(0); \quad \rho_{bd}(0) = \sum_k D_{bd}^{kk}(0) \end{aligned} \quad (9)$$

where P_k is the steady-state (with respect to exciton relaxation) population of the k th one-exciton state, $\rho_{ca}(\tau)$ and $\rho_{bd}(\tau)$ are vibrational density matrixes for the ground and excited states. Note that when calculating the doorway and window amplitudes in eqs 6 we have assumed that the pump and probe pulses are

shorter than the time scale of exciton and vibrational relaxation. In eqs 9 the initial doorway amplitudes contain the trace over the exciton states, so that the result does not depend on the exciton relaxation during the pulse. This implies that eqs 9 are valid for any arbitrary relation between the pulse duration and the exciton relaxation time scale, but the pump–probe delay τ must be larger than these two times.

The time evolution of the vibrational density matrixes can be obtained using the Liouville equation with the Redfield relaxation tensor.^{54,66} In the case of a single vibrational mode we have

$$\begin{aligned} \dot{\rho}_{bd} &= -i(\omega_b - \omega_d)\rho_{bd} - \tilde{\gamma}(b-d)^2\rho_{bd} - \gamma/2[b+d+(2+b+d)\exp(-\beta\Omega)]\rho_{bd} - \tilde{\gamma}/2[b(b-1)+d(d-1)+((b+2)(b+1)+(d+2)(d+1))\exp(-2\beta\Omega)]\rho_{bd} + \\ &\quad \gamma\sqrt{(b+1)(d+1)}\rho_{b+1,d+1} + \\ &\quad \tilde{\gamma}\sqrt{(b+1)(b+2)(d+1)(d+2)}\rho_{b+2,d+2} + \gamma\sqrt{bd}\exp(-\beta\Omega)\rho_{b-1,d-1} + \tilde{\gamma}\sqrt{b(b-1)d(d-1)}\exp(-2\beta\Omega)\rho_{b-2,d-2} \end{aligned} \quad (10)$$

where Ω is the vibrational frequency; $\omega_b = \Omega(b + 1/2)$, $b = 0, 1, 2, \dots$; $\beta = 1/(k_B T)$; k_B is the Boltzmann constant, T is the temperature; $\gamma, \tilde{\gamma}$ are the time constants for one- and two-phonon relaxation; $\tilde{\gamma}$ is the constant of pure dephasing. The time evolution of $\rho_{ca}(\tau)$ is given by eq 10 by changing $b \rightarrow c, d \rightarrow a$ and by taking the appropriate values for $\Omega, \gamma, \tilde{\gamma}$, and $\tilde{\gamma}$ (in general, these parameters are different for the ground and excited states).

In the case of two vibrational modes the index b in eqs 5–9 takes the values $\{b_1 b_2\}$, $b_1 = 0, 1, 2, \dots, b_2 = 0, 1, 2, \dots$; the vibrational energy is $\omega_b = \omega_{b_1} + \omega_{b_2}$; $\omega_{b_1} = \Omega_1(b_1 + 1/2)$, $\omega_{b_2} = \Omega_2(b_2 + 1/2)$, where Ω_1 and Ω_2 are the relevant vibrational frequencies; $\langle b|a \rangle = \langle b_1|a_1 \rangle \langle b_2|a_2 \rangle$. The vibrational density matrix is $\rho_{bd}(\tau) = \rho_{b_1 d_1}(\tau) \rho_{b_2 d_2}(\tau)$, where $\rho_{b_1 d_1}(\tau)$ and $\rho_{b_2 d_2}(\tau)$ are given by eq 10 with parameters $\omega_{b_1}, \Omega_1, \gamma_1, \tilde{\gamma}_1, \tilde{\gamma}_1$ or $\omega_{b_2}, \Omega_2, \gamma_2, \tilde{\gamma}_2, \tilde{\gamma}_2$ instead of $\omega_b, \Omega, \gamma, \tilde{\gamma}, \tilde{\gamma}$. Similarly, the ground-state density matrix is $\rho_{ca}(\tau) = \rho_{c_1 a_1}(\tau) \rho_{c_2 a_2}(\tau)$.

The steady-state pump–probe spectrum $\Delta A(\omega_2)$ corresponding to time delays longer than the time scales of exciton and vibrational relaxation is given by eq 9 with

$$\begin{aligned} \rho_{bd}(\tau) &\rightarrow \delta_{bd} P_b \text{OD}(\omega_1); \quad \rho_{ca}(\tau) \rightarrow \delta_{ca} P_a \text{OD}(\omega_1) \\ \text{OD}(\omega_1) &= \sum_{k,b} D_{bb}^{kk}(0, \omega_1) \equiv \sum_a D_{aa}^{gg}(0, \omega_1) \end{aligned} \quad (11)$$

where OD is the linear absorption of the pump pulse. When the pulse duration τ_1 is comparable with the electronic dephasing time scale, the OD spectrum depends on τ_1 . Typically the OD spectrum is measured by a continuous light source. This situation corresponds to the $\tau_1 \rightarrow \infty$ limit of eqs 6, 8, and 11. Notice, that in general the steady-state pump–probe spectrum $\Delta A(\omega_2)$ is dependent on the pulse durations τ_1, τ_2 , and excitation frequency ω_1 .

Model of Antenna

Geometry of Antenna and Electronic Hamiltonian. The elementary subunit of the core antenna of *Rps. viridis* consists

of three transmembrane polypeptides α , β and γ .^{67–69} The α and β polypeptides, binding one BChl molecule each, are analogous to the LH1 proteins found in BChl *a*-containing bacteria. The γ -polypeptide probably does not bind BChl.⁶⁸ The available structural information suggests that the photosynthetic unit of *Rps. viridis* consists of one reaction center surrounded by six antenna subunits ($\alpha_2\beta_2\gamma_2$ BChl₄) (each containing two α , two β , two γ polypeptides, and four BChls) arranged in a ringlike structure with 6-fold symmetry.^{67–69} The spatial arrangement of the BChls should have at least the same (6-fold) or even higher (12-fold) symmetry (the exact information about the BChl organization in this antenna complex is not known). Alternatively, the LH1 may be a 16-fold symmetric ring of 16 ($\alpha\beta\gamma$ BChl₂) subunits, as was shown to be the case for the BChl *a* containing species.^{6,70} In this case the spatial arrangement of the BChls should also exhibit 16-fold symmetry. Recent 10 Å resolution studies of reaction center-LH1 complex of *Rps. viridis*⁷¹ suggested that the pigments in the antenna are arranged in a ringlike structure at approximately equal distances from the geometrical center of the complex. However, the data gave no information about the symmetry of the BChl arrangement in the ring.

We assume that the pigment arrangement in the antenna of *Rps. viridis* is analogous to that of the BChl *a*-containing bacteria. As a model for the antenna of *Rps. viridis* we consider a circular aggregate of $N = 24$ or $N = 32$ BChl *b* molecules with either C₁₂ or C₁₆ symmetry (the elementary unit cell contains two BChl *b* molecules, bound to the α and β polypeptides). The Q_y transition dipole moments of the two BChls in a dimeric unit cell form angles ψ_1, ψ_2 with the plane of the circle and angles φ_1, φ_2 with the tangent to the circle. The Mg–Mg distance between BChls in a dimeric unit is r_{12} and between nearest BChls from different units is r_{23} . We further assume that $\psi_1 = 10^\circ$, $\psi_2 = 5^\circ$, $\varphi_1 = 20^\circ$, $\varphi_2 = 200^\circ$, $r_{12} = 0.87$ nm, $r_{23} = 0.97$ nm. These parameters are approximately the same as those for the strongly coupled B850 ring of BChl *a*'s in the LH2 antenna from *Rps. acidophila*.⁵ We have furthermore taken the interaction energies between BChl *b* molecules as $M_{12} = 400$ cm⁻¹, $M_{23} = 290$ cm⁻¹, $M_{13} = -52$ cm⁻¹, and $M_{14} = 14$ cm⁻¹, where M_{12} corresponds to the intradimer interactions, M_{23} to interdimer nearest-neighboring interactions, M_{13} to second neighbors interactions, and M_{14} to third neighbors interactions. The unperturbed Q_y electronic transition energies of the two BChls in a dimeric unit cell are E_1 and E_2 . The difference between E_1 and E_2 was taken to be 300 cm⁻¹. The site inhomogeneity of the LH1 antenna was described by uncorrelated perturbations δE to E_1 and E_2 (uncorrelated diagonal disorder). The δE values were randomly taken from a Gaussian distribution $W(\delta E) = \pi^{-1/2}\Delta^{-1}\exp(-\delta E^2/\Delta^2)$. The width (fwhm) of this distribution is $\sigma = 2\Delta(\ln 2)^{1/2}$.

In our earlier work⁴⁷ we have shown that this model allows to explain the shapes of linear absorption and pump–probe spectra of the core antenna of *Rps. viridis*. It was shown that the model is not very sensitive to a variation of the geometry (asymmetry in the intra- and interdimer distances r_{12} and r_{23} , a variation of the antenna size N or a breaking of the closed ring by removing one or two dimeric subunits). In this work we have used a fixed geometry (with $N = 24$) and fixed parameters of the electronic Hamiltonian (i.e., diagonal energies E_1, E_2 and off-diagonal couplings $M_{12}, M_{23}, M_{13}, M_{14}$). The diagonal disorder value σ is variable.

Note that in our previous work⁴⁷ we considered the Bchl *b* molecules as three-level systems. The relative contribution of

double-excited monomeric states to the difference absorption of an aggregate is about χ^2/N_{eff} , where χ is the ratio of the S_1 – S_2 and S_0 – S_1 transition dipoles in BChl monomer, and N_{eff} is the delocalization length of individual exciton wave functions. Typically, the value of χ is taken to range from 0.3 to 1.0.^{45,47,72,73} This implies that for small-size aggregates χ^2/N_{eff} may be significant (up to 50%). But for the LH1 antenna of *Rps. viridis* $N_{\text{eff}} = 6$ –10 at 77 K and $\chi = 0.5$,⁴⁷ so that χ^2/N_{eff} is no more than 4% (as can be confirmed by direct numerical calculation). This allows us to restrict ourselves to a two-level scheme. The vibrational structure of an aggregate of three-level molecules is much more complicated as was demonstrated for a dimer in refs 55 and 56.

Parameters of Vibrational Modes. We suppose that electronic transitions are coupled to two vibrational modes with the frequencies Ω_1 and Ω_2 and relaxation constants $\gamma_1, \tilde{\gamma}_1, \bar{\gamma}_1$ and $\gamma_2, \tilde{\gamma}_2, \bar{\gamma}_2$. These parameters are assumed to be the same for the ground state, one-exciton, and two-exciton states. The vibrational modes are represented as harmonic oscillators with the ground-state wave functions $\varphi_{a1}(Q_1)$ and $\varphi_{a2}(Q_2)$, where Q_1 and Q_2 are nuclear coordinates. The excited-state wave functions are $\varphi_{b1}(Q_1 - \Delta_1)$ and $\varphi_{b2}(Q_2 - \Delta_2)$, where Δ_1 and Δ_2 are the oscillator displacements. The corresponding Huang–Rhys factors which determine the overlap of vibrational states $\langle b_1|a_1 \rangle$ and $\langle b_2|a_2 \rangle$ are $S_1 = (\Delta_1)^2/2$ and $S_2 = (\Delta_2)^2/2$. According to eq 2 the wave functions associated with the two-exciton states are $\varphi_{f1}(Q_1 - 2\Delta_1)$ and $\varphi_{f2}(Q_2 - 2\Delta_2)$. We also have studied the case when the relative displacement of the two-exciton states is of opposite sign with respect to that of the one-exciton states, so that the two-exciton wave functions are $\varphi_{f1}(Q_1)$ and $\varphi_{f2}(Q_2)$.

The dynamics of the vibrational wave packets in the ground and excited state is given by

$$\begin{aligned}\Psi_g(Q_1, Q_2, \tau, \omega_1) &= \sum_{\substack{a=\{a_1, a_2\} \\ c=\{c_1, c_2\}}} \varphi_{c1}(Q_1)\varphi_{a1}(Q_1)\varphi_{c2}(Q_2)\varphi_{a2}(Q_2) \times \\ &\quad \rho_{ca}(\tau, \omega_1) \\ \Psi_e(Q_1, Q_2, \tau, \omega_1) &= \sum_{\substack{d=\{d_1, d_2\} \\ b=\{b_1, b_2\}}} \varphi_{b1}(\tilde{Q}_1)\varphi_{d1}(\tilde{Q}_1)\varphi_{b2}(\tilde{Q}_2)\varphi_{d2}(\tilde{Q}_2) \times \\ &\quad \rho_{bd}(\tau, \omega_1) \\ \tilde{Q}_1 &= Q_1 - \Delta_1; \quad \tilde{Q}_2 = Q_2 - \Delta_2\end{aligned}\quad (12)$$

In the model we have assumed that the time evolution of the vibrational density matrix $\rho_{bd}(\tau)$ does not depend on exciton relaxation or/and migration in the antenna. However, the dephasing of the ground- and excited-state vibrational wave packets are slightly different (as revealed by fitting of the experimental data, see below). We therefore suppose that the time evolution of the excited-state density matrix is given by $\rho_{bd}(\tau) \exp(-(1 - \delta_{bd})\tau/\tau_{\text{hop}})$, where $\rho_{bd}(\tau)$ does not depend on the electronic coordinates and τ_{hop} is some phenomenological constant describing the additional slow decay of the vibrational coherences. Most probably, the physical origin of this additional dephasing is connected with the incoherent motion of the quasi-steady-state exciton (polaron) around the ringlike antenna.

Dephasing of the Exciton-Vibrational Transitions. The dephasing of the electronic transitions is characterized by the rates Γ and Λ (see eq 7). Typically, the higher states are broadened due to fast relaxation, whereas the lowest one may have a relatively long lifetime, especially at low temperature. That is why we introduced different dephasing rates, corresponding to transitions from the ground state to the lowest one-

exciton state (Γ_{1L} , Λ_{1L}), from the ground to higher one-exciton states (Γ_{1H} , Λ_{1H}), from the lowest one-exciton state to the two-exciton states (Γ_{2L} , Λ_{2L}), and from the higher one-exciton to two-exciton states (Γ_{2H} , Λ_{2H}). We supposed that the ratio Γ_i/Λ_i is approximately the same for all transitions. The total dephasing rate for any exciton–vibrational transition is the sum of the electronic and vibrational dephasing rates. For example, for the transition from the a th sublevel of the ground state to the b th sublevel of the lowest one-exciton state we have $\Gamma_{1L} + (\Gamma_a + \Gamma_b)/2$, where Γ_a is the width (fwhm) of the corresponding vibronic sublevel. According to eq 10

$$\Gamma_d/2 = \gamma_1[a_1 + (1 + a_1)\exp(-\beta\Omega_1)] + \tilde{\gamma}_1[a_1(a_1 - 1) + (a_1 + 2)(a_1 + 1)\exp(-2\beta\Omega_1)] + \gamma_2[a_2 + (1 + a_2)\exp(-\beta\Omega_2)] + \tilde{\gamma}_2[a_2(a_2 - 1) + (a_2 + 2)(a_2 + 1)\exp(-2\beta\Omega_2)] \quad (13)$$

There is no vibrational contribution to Λ_{1L} because in our model we have only exponential decay of the vibronic sublevels (see eq 10).

Results

Model System: Three Electronic Levels and One Vibrational Mode. We start with a simple example of a system which has a ground state, a single one-exciton state and a single two-exciton state. (Such a model can be used for a dimer of two-level molecules if higher one-exciton state is forbidden and well separated from the lower one). The frequency of the one- to two-exciton transition is 180 cm^{-1} larger than that of the ground to one-exciton transition. Both transitions have the same electronic dephasing constants ($\Gamma_{1L} = \Gamma_{2L} = 80\text{ cm}^{-1}$, $\Lambda_{1L} = \Lambda_{2L} = 0$) and the same dipole strengths. The three states are coupled to a single vibrational mode with the parameters $\Omega = 100\text{ cm}^{-1}$, $\gamma = 15\text{ cm}^{-1}$, $\tilde{\gamma} = 0$, $\bar{\gamma} = 0$, $S = 0.8$. The pump and probe pulse duration is 70 fs (fwhm). We have modeled the 77 K kinetics with the excitation energies $\omega_1 = 300, 0$, and -150 cm^{-1} , corresponding to the blue side, maximum, and the red side of the absorption band, respectively (the energies ω_1 and ω_2 are counted from the energy of the zero-phonon ground to one-exciton transition).

The ground and one-exciton potential curves are shown in Figure 1 together with the vibrational wave packets for the different excitation conditions. The ground- and excited-state wave packets are shown for five different delays τ corresponding to the first half-period of the wave packet oscillations. Upon short-wavelength excitation both wave packets oscillate in phase, while after long-wavelength excitation they oscillate out of phase. When the excitation frequency corresponds to the absorption maximum (ω_1 is between 0 and $\Omega/2$ in the case of $S < 1$) the ground-state wave packet displays a phase shift of about $\pi/2$. The oscillations in the ground state are responsible for the oscillatory features of the PB component, whereas the oscillations of the excited-state wave packet determine the oscillatory dynamics of the ESA and SE (Figure 2). The ESA dynamics depends on the displacement of the two-exciton potential curve with respect to the one-exciton potential. We consider two cases with the relative displacement of the two-exciton potential of the (i) same and (ii) opposite sign as compared to the one-exciton displacement. The corresponding ESA and ΔA spectra are labeled as ESA_{\pm} and ΔA_{\pm} .

The oscillations of the SE, PB, and ESA_{\pm} components have some common features (Figure 2). If we look at the time dependencies, for example, $\text{SE}(\tau)$ at fixed probe frequencies ω_2 , we find that oscillations have opposite phases on the blue

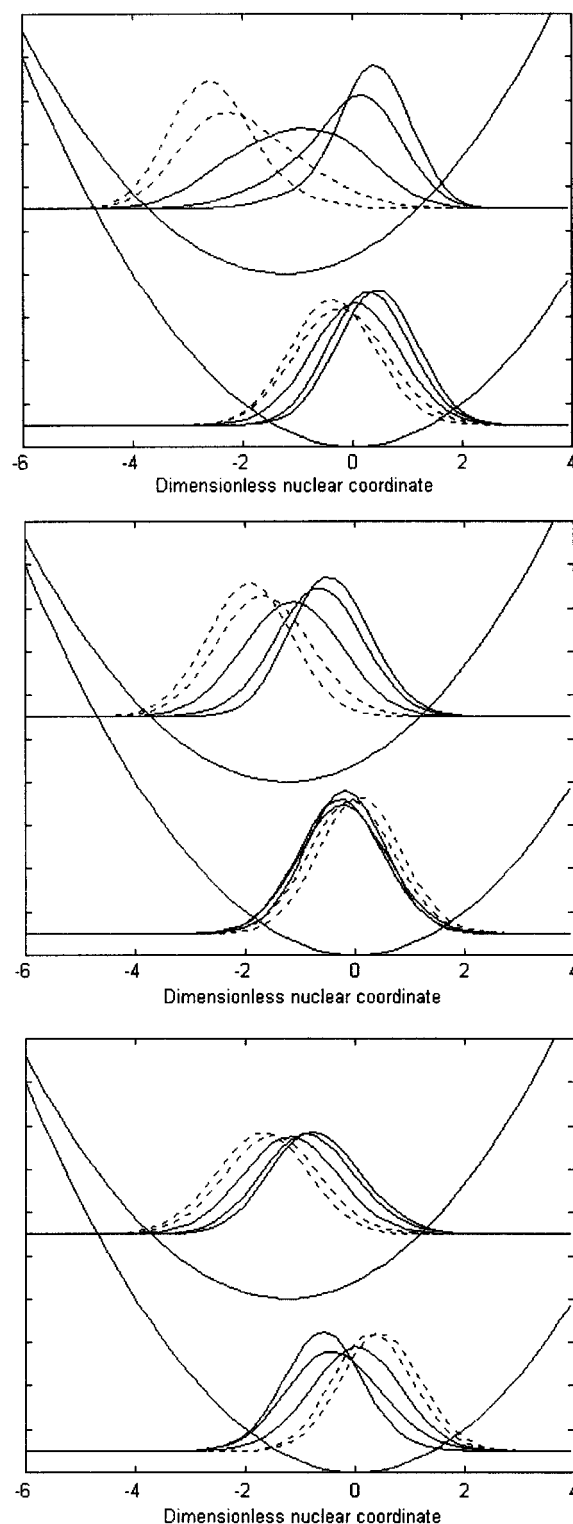


Figure 1. Ground and one-exciton potential curves and the vibrational wave packets for the three-level model following three different excitation frequencies. Pulse duration is 70 fs, $T = 77\text{ K}$, $\omega_1 = 300$ (top frame), 0 (middle frame), and -150 cm^{-1} (bottom frame). The ground- and excited-state wave packets are shown for delays $\tau = 0, 38, 76$ (solid lines), 114, 152 fs (dashed lines), corresponding to the first half-period (167 fs) of the wave packet oscillations. Parameters of the vibrational mode and electronic dephasing are $\Gamma_{1L} = \Gamma_{2L} = 80\text{ cm}^{-1}$, $\Lambda_{1L} = \Lambda_{2L} = 0$, $\Omega = 100\text{ cm}^{-1}$, $\gamma = 15\text{ cm}^{-1}$, $\tilde{\gamma} = 0$, $\bar{\gamma} = 0$, $S = 0.8$.

and red side of the SE band with a reversion of the phase close to the middle of the SE band. Near this phase reversion point the amplitude of oscillations with the main frequency Ω vanishes

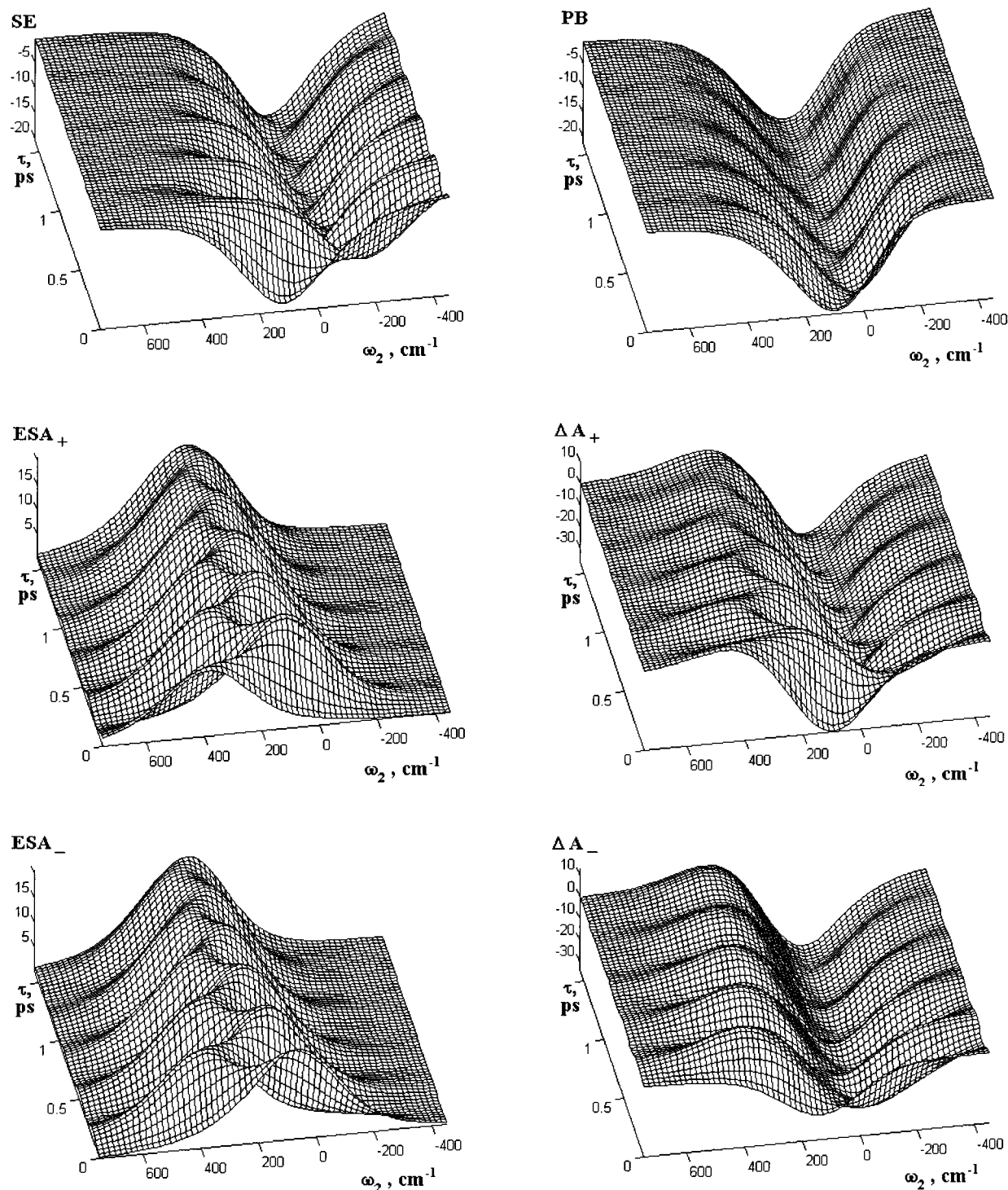


Figure 2. Time-dependent PB, SE, and ESA and resulting ΔA spectra for the three-level model system upon short-wavelength excitation, $\omega_1 = 300 \text{ cm}^{-1}$. The ESA_\pm and ΔA_\pm spectra correspond to positive and negative relative displacement of the two-exciton potential curve. All parameters are the same as in Figure 1.

and oscillations with double frequency (2Ω) appear. Note that the phase of the main frequency oscillations shows no shift when ω_2 is changed from the blue to the red side of the band, but there is a quick phase jump in the middle of the band. The ESA and SE oscillations have the same form, because both the ESA and SE components are determined by the excited state wave packet dynamics. The only difference is the opposite sign of the amplitudes and the 180 cm^{-1} blue shift of the ESA. If we invert the $\text{SE}(\tau, \omega_2)$ surface it would look identical to the $\text{ESA}_-(\tau, \omega_2)$. The ESA_- and ESA_+ surfaces are the same, but have the opposite phases for the oscillations. The oscillations

of the PB component upon blue-side excitation are the same as those of the SE, but have smaller amplitude (see also Figure 1, top frame).

The superposition of the three components, SE, ESA, and PB, results in a complicated time dependence of the total difference absorption ΔA (Figure 2). The phase of the oscillations is determined by the ESA component in the short-wavelength positive wing, by the PB/SE near the negative bleaching peak, and by the SE component in the long-wavelength negative wing. In the case of short-wavelength excitation (shown in Figure 2) these three regions are separated

by the two phase-inversion points for the ΔA_+ spectrum. The ΔA_- spectrum has only one phase reversion point (when the blue shift of the ESA spectrum is small, as shown in Figure 2) or three reversion points (if the ESA shift exceeds 400 cm^{-1} , data not shown). Notice that the phase of the oscillations in the short-wavelength wing is determined only by the ESA contribution, giving a direct indication about the sign of the two-exciton state displacement. Another possibility to distinguish between the (+) and (−) configurations is to compare the phases in the blue wing and very red wing of the spectrum. The latter is determined by the SE phase which is independent of the two-exciton displacement. The phases should be the same for the (+) configuration and opposite for the (−) one.

In Figure 2 we have shown the spectra for short-wavelength excitation. For the other excitation conditions we will have approximately the same character of the SE and ESA components, but very different PB components. Upon long-wavelength excitation we will have the opposite phase of oscillations of the PB component (see Figure 1, bottom frame). Because of the relatively small amplitude of the PB oscillations, the total spectrum ΔA will be approximately the same as shown in Figure 2, but the phase-reversion point near the bleaching peak will be shifted to the red (data not shown). In the case of the $\pi/2$ phase shift of the PB oscillations upon middle-band excitation (Figure 1, middle frame) we will observe a gradually shifting phase as we approach the peak of the bleaching instead of a quick phase reversal (Figure 3).

The origin of the fast phase reversions vs gradually increasing shifts can be illustrated by a simple example. For the red- and blue-side excitations the oscillatory part of the signal will be composed of a sum of components like $A_1 \sin(\Omega\tau + \pi) + A_2 \sin(\Omega\tau)$, where A_1 and A_2 are wavelength-dependent amplitudes. The resulting oscillations will always have the phase of 0 or π (depending on the ratio of A_1 and A_2). However, for middle-band excitation we will have the sum $A_1 \sin(\Omega\tau + \pi/2) + A_2 \sin(\Omega\tau)$ which is equal to $\sin[\Omega\tau + \varphi(A_1, A_2)]$, where $\varphi(A_1, A_2)$ is the wavelength-dependent phase. This explains the wavelength-dependent kinetics shown in Figure 3. Notice that some nonlinear distortion of the sinuslike oscillations occurs near the points of phase reversion or shift (Figure 3), which is due to the presence of the double-frequency components near these points.

The results of this subsection were obtained using a vibronic state representation. In this approach the nontrivial phase shift of the PB component is connected with the imaginary part of the ground state doorway amplitude $D_{ca}^{gg}(0)$ due to $P_a \neq P_c$ (see eqs 6). To make sure that these phase-shift effects are not due to limitations of our model, we also have used a more general eigenstate-free approach based on the cumulant expansion.⁵¹ Approaching the phonon spectral density by a low-frequency overdamped mode plus a 100 cm^{-1} underdamped mode, and using the expressions for the nonlinear response of the two- and three-level systems,^{51,61,62} we were able to reproduce all special features of the kinetics discussed here and shown in Figures 1–3.

Core LH1 Antenna of *Rps. viridis*. Now we switch to modeling the core LH1 antenna of *Rps. viridis*. Our goal is to quantitatively explain the linear and nonlinear absorption spectra as well as the transient absorption kinetics obtained in experiments.²⁹ In this paper we restrict ourselves to fitting the data obtained at 77K. This data includes three sets of pump–probe kinetics at different detection wavelength (990–1090 nm) obtained with 100 fs pulses upon excitation at 1017, 1036, and

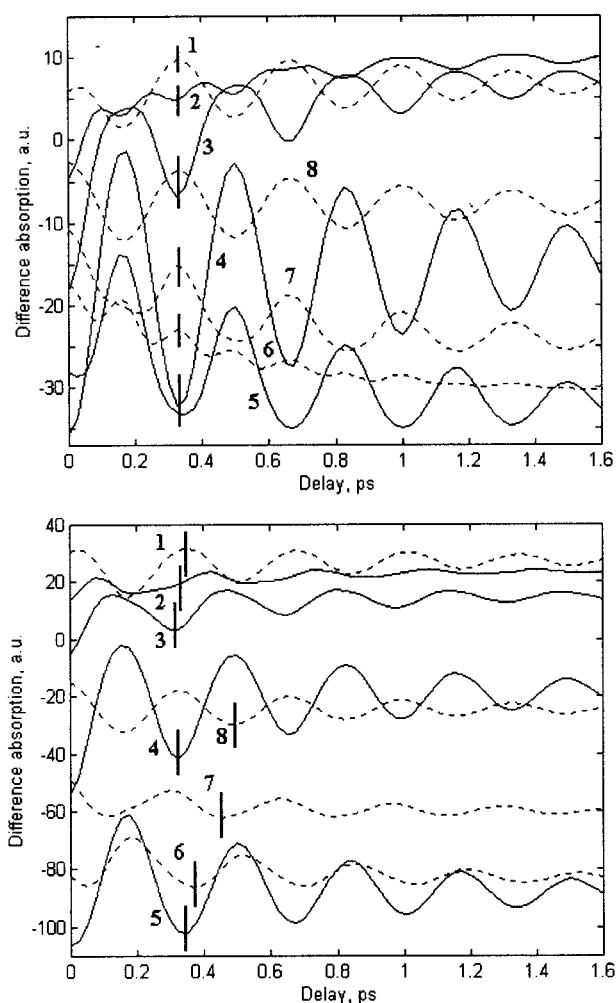


Figure 3. Pump–probe kinetics for the three-level model at two excitation frequencies, $\omega_1 = 300\text{ cm}^{-1}$ (top frame) and 0 (bottom frame) and different detection frequencies: $\omega_2 = 431, 319, 244, 112, 0, -75, -131, -300\text{ cm}^{-1}$ (for curves 1–8, top frame) and $\omega_2 = 319, 263, 225, 150, 0, -75, -150, -281\text{ cm}^{-1}$ (for curves 1–8, bottom frame). Curves 1 and 6–8 are shown by dashed lines, curves 2–5 are shown by solid lines. The two-exciton state displacement is positive; all other parameters are the same as in Figure 1. Vertical bars mark the maxima and/or minima in the oscillatory kinetics to highlight the effects of the phase reversion and phase shift.

1055 nm, corresponding to the blue side, the region near maximum, and the red side of the absorption band.

In our modeling the geometry of antenna is fixed as well as the interaction energies $M_{12} = 400\text{ cm}^{-1}$, $M_{23} = 290\text{ cm}^{-1}$, $M_{13} = -52\text{ cm}^{-1}$, $M_{14} = 14\text{ cm}^{-1}$, and the intradimer asymmetry $E_1 - E_2 = 300\text{ cm}^{-1}$. The free parameters are (i) the site inhomogeneity σ ; (ii) the line-broadening widths Γ_{1L} , Γ_{1H} , Γ_{2L} , Γ_{2H} , Λ_{1L} , Λ_{1H} , Λ_{2L} , Λ_{2H} ; (iii) the parameters of two vibrational modes Ω_1 , Ω_2 , S_1 , S_2 , γ_1 , $\tilde{\gamma}_1$, γ_2 , $\tilde{\gamma}_2$; and (iv) the effective hopping constant τ_{hop} . These free parameters should be determined from the simultaneous fit of the linear absorption, steady-state pump–probe spectra, and three sets of pump–probe kinetics upon excitation at 1017, 1036 and 1055 nm. These fits are shown in Figures 4–7.

The vibrational frequencies and Huang–Rhys factors can be precisely determined by fitting the shape of the oscillatory patterns (positions and amplitudes of the maxima and minima). The decay of the oscillations at different detection wavelengths (i.e., with different contribution of the PB, SE, and ESA) gives information about the relaxation constants (for the ground and excited states) and hopping constant (for the excited state).

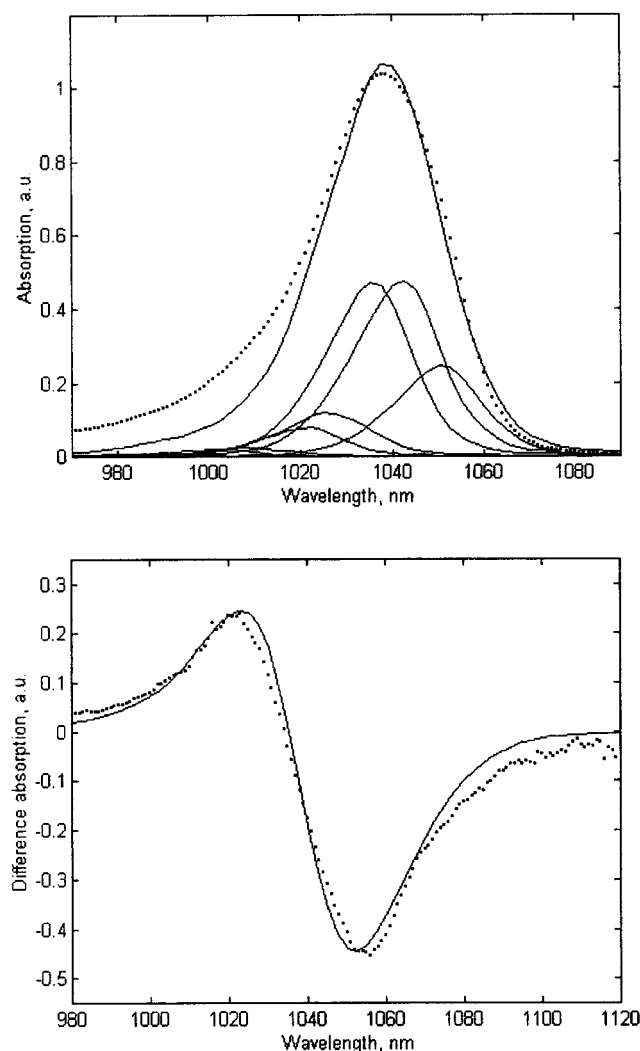


Figure 4. Simultaneous fit of linear absorption (top) and pump-probe spectra (bottom). Points show experimental data; solid lines show the calculated spectra. The calculated linear absorption is shown together with its components corresponding to individual exciton states. $T = 77$ K, $N = 24$, the interaction energies are $M_{12} = 400$ cm^{-1} , $M_{23} = 290$ cm^{-1} , $M_{13} = -52$ cm^{-1} , and $M_{14} = 14$ cm^{-1} , the site inhomogeneity $\sigma = 440$ cm^{-1} , the electronic dephasing constants: $\Gamma_{1L} = 2$ cm^{-1} , $\Gamma_{1H} = 10$ cm^{-1} , $\Gamma_{2L} = 8$ cm^{-1} , $\Gamma_{2H} = 12$ cm^{-1} , $\Lambda_{1L} = 10$ cm^{-1} , $\Lambda_{1H} = 45$ cm^{-1} , $\Lambda_{2L} = 35$ cm^{-1} , $\Lambda_{2H} = 55$ cm^{-1} ; parameters of two vibrational modes: $\Omega_1 = 58$ cm^{-1} , $\Omega_2 = 110$ cm^{-1} , $S_1 = 0.41$, $S_2 = 0.23$, $\gamma_1 = 11$ cm^{-1} , $\gamma_2 = 11$ cm^{-1} , $\tau_{\text{hop}} = 1.2$ ps. The relative oscillator displacement of the two-exciton states is positive for both nuclear coordinates.

Leegwater⁶⁶ suggested that the oscillatory shapes for RCs, especially near the phase reversion points, can be better explained by including a nonlinear relaxation process. In our case we were able to satisfactory fit the oscillatory traces in the linear approximation, implying that $\tilde{\gamma}_1 \approx \tilde{\gamma}_2 \approx \tilde{\gamma}_3 \approx \tilde{\gamma}_4 \approx 0$. The phase of the oscillations in the blue wing of the difference spectrum allowed us to unambiguously determine the displacement of two-exciton states as the (+) configuration for both nuclear coordinates, i.e., the absolute displacements are $2\Delta_1$ and $2\Delta_2$ as suggested by eq 2. The site inhomogeneity and line-broadening widths can be obtained by fitting the spectral shapes of the linear and difference absorption. Of course, these spectral shapes are also dependent on the vibrational parameters as well as that the oscillatory features are dependent on the site inhomogeneity and line broadening parameters. A self-consistent fit (Figures 4–7) was obtained for $\sigma = 440$ cm^{-1} , $\Gamma_{1L} = 2$

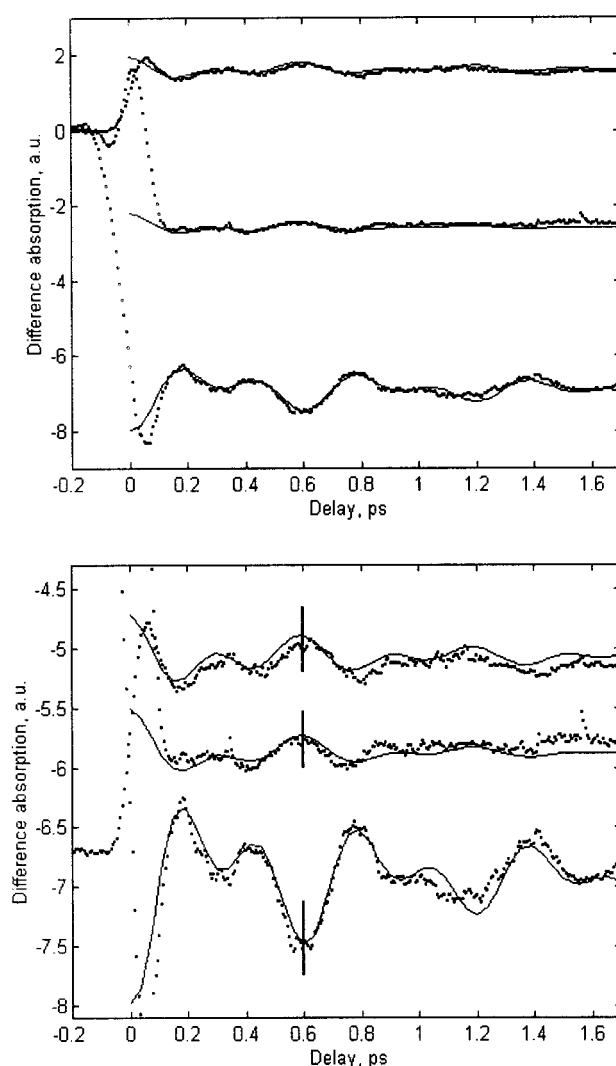


Figure 5. Experimental (points) and calculated (solid lines) pump-probe kinetics at 77 K upon excitation at 1055 nm (top frame). Detection wavelengths are (from top to bottom): 1010, 1070, and 1050 nm. All parameters are the same as in Figure 4. The bottom frame shows the same data, but curves are shifted in vertical direction to make comparison easy.

$\Gamma_{1H} = 10$ cm^{-1} , $\Gamma_{2L} = 8$ cm^{-1} , $\Gamma_{2H} = 12$ cm^{-1} , $\Lambda_{1L} = 10$ cm^{-1} , $\Lambda_{1H} = 45$ cm^{-1} , $\Lambda_{2L} = 35$ cm^{-1} , $\Lambda_{2H} = 55$ cm^{-1} , $\Omega_1 = 58$ cm^{-1} , $\Omega_2 = 110$ cm^{-1} , $S_1 = 0.41$, $S_2 = 0.23$, $\gamma_1 = 11$ cm^{-1} , $\gamma_2 = 11$ cm^{-1} , $\tau_{\text{hop}} = 1.2$ ps. These values are determined from the fit with an accuracy of $\pm 5\%$ (σ), $\pm 10\%$ (Λ), $\pm 4\%$ (Ω_1 , Ω_2), $\pm 10\%$ (S_1 , S_2), $\pm 10\%$ (γ_1 , γ_2), $\pm 25\%$ (τ_{hop}). The ratio of Lorentzian and Gaussian line broadening Λ_i/Γ_i should not be taken less than 4 to fit the line shape. As a result, the Γ_i values are too small and cannot be determined precisely. We assumed that $\Gamma_i \approx \Lambda_i/4.5$. Notice that our vibrational frequencies (58, 110 cm^{-1}) are close to those obtained from the fitting of experimental kinetics by a damped sinusoidal functions (61, 106 cm^{-1}) and from the FT spectrum of the kinetics (65, 103 cm^{-1}).²⁹

It is important that the coupling parameter $\kappa = (\Omega_1 S_1 + \Omega_2 S_2)/(2M_{12} + 2M_{23})$ which determines the size of the polaron^{57–59} is 0.036 thus corresponding to the large polaron limit ($\kappa \ll 1$), as was assumed in our theoretical model.

Figure 4 shows fits of the linear and difference absorption profiles. A more or less satisfactory fit of the spectra can be obtained by choosing different contributions of Lorentzian and Gaussian line broadening to a Voigt profile for each of the

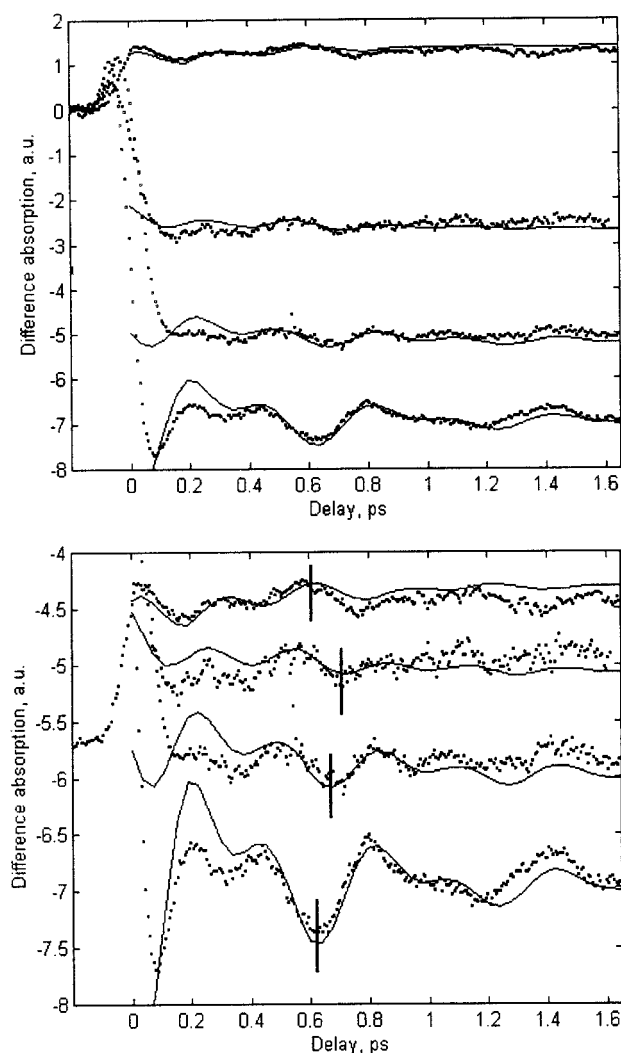


Figure 6. The same as in Figure 5, but for excitation at 1036 nm and detection (from top to bottom): 1010, 1070, 1060, and 1050 nm.

individual exciton–vibrational transitions. In the case of a Lorentzian line shape ($\Lambda = 0$) the fit of the linear absorption becomes better at shorter wavelength, whereas the Gaussian limit ($\Gamma = 0$) allows a better fit of the long-wavelength wing. We found that the shape of the red wing is much more critical because of its strong influence on the pump–probe kinetics in the PB/SE region and that is why $\Gamma \ll \Lambda$ was chosen in our fit. Notice that we are not able to quantitatively fit the short-wavelength tail of the absorption because we use the two-mode limit without taking into account the coupling to high frequency ($> 150 \text{ cm}^{-1}$) vibrational modes (for more than two modes the eigenstate representation is unpractical).

The fit of the pump–probe kinetics looks very good for the 1055 nm excitation (Figure 5). These kinetics are not significantly influenced by exciton relaxation because the initially created exciton populations are very close to the steady-state limit. We remind that our theory is valid for time delays longer than the exciton relaxation time scale (300–400 fs for complete relaxation with a 150 fs time constant) and the time interval of pump–probe overlap (100–150 fs). Upon excitation at 1055 nm we obtained a good fit even at delays as short as 100 fs. Upon short-wavelength excitation (Figures 6 and 7) there are some discrepancies below 300–400 fs, and also small deviations of the calculated curves at delays longer than 1 ps compared with the experimental data. The latter can be compensated by introducing some additional decay of the ΔA with a time

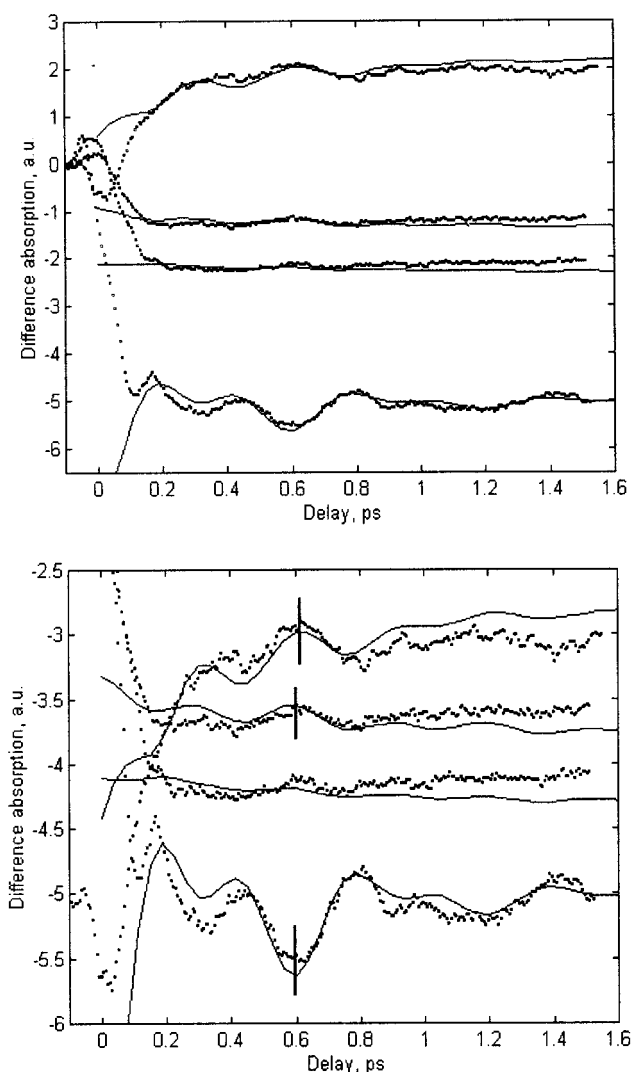


Figure 7. The same as in Figure 5, but for excitation at 1017 nm and detection (from top to bottom): 1020, 1080, 1070, and 1050 nm.

constant of 5–15 ps (data not shown). This long decay may reflect the energy migration between different circular antenna units in the membrane or some kind of trapping process.

Both calculated and measured kinetics show the time-dependent shift of the zero level (nonoscillatory part) of the kinetics upon short-wavelength excitation, which is connected with vibrational relaxation and downhill energy transfer. Concerning the former, short-wavelength excitation creates a nonequilibrium vibrational population in the excited state (Figure 1, top frame), giving rise to a dynamic Stokes shift of the SE and anti-Stokes shift of the ESA spectra. As a result, we have an increase with time of the ΔA value in the blue and in the red wings of the difference spectrum, which only occurs upon short-wavelength excitation. This effect takes place in our model system (compare the top and bottom frames of Figure 3) and in the LH1 antenna (compare the 1010 nm kinetics in Figures 5 and 6 and 1020 nm kinetics in Figure 7). Note that for LH1 this effect is clearly seen in the ESA region, but remains hidden in the PB/SE region, because the SE contribution in the ringlike antenna is relatively weak as compared to PB, corresponding to about 15% of the total dipole strength of an aggregate.^{47,74}

It is also interesting to compare the wavelength-dependent phase of the oscillations following the different excitation conditions (Figures 5–7). Upon red-side and blue-side excitation (Figures 5 and 7) there are two phase-reversion points: between

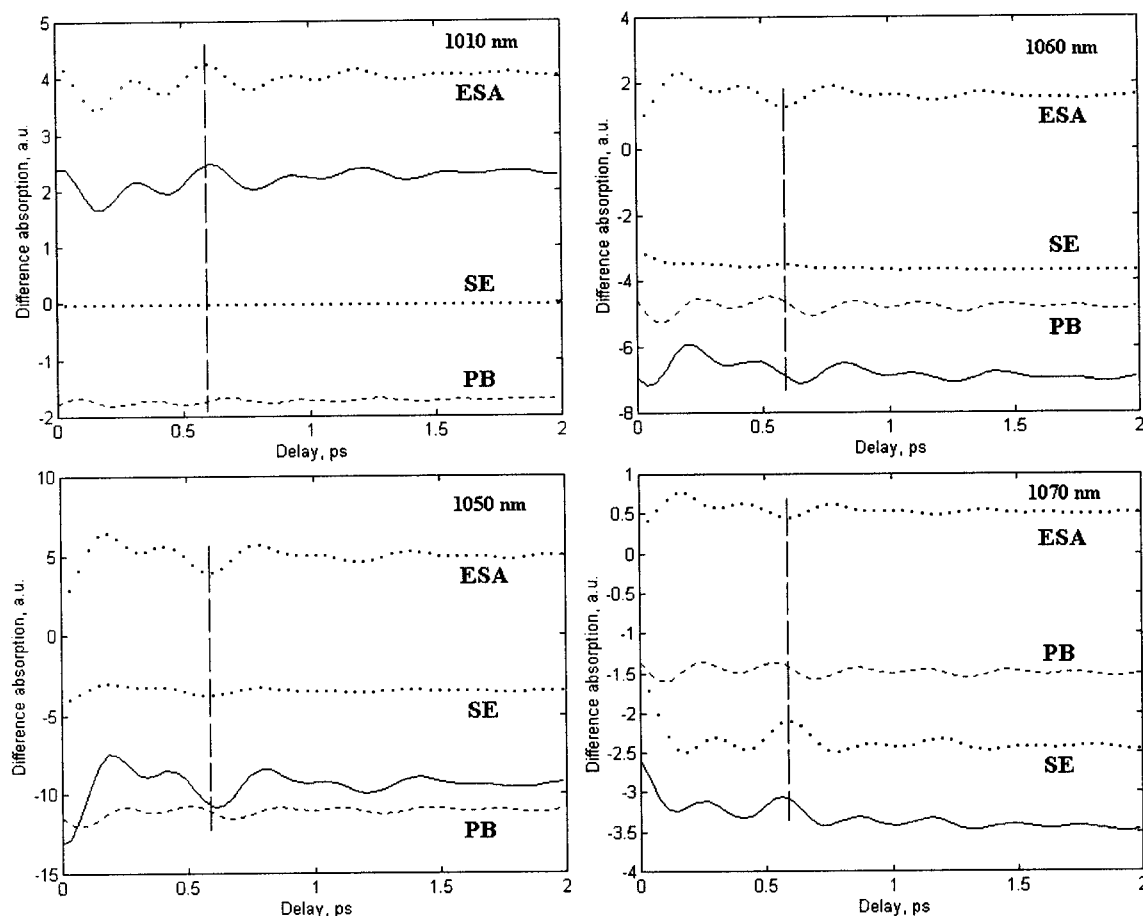


Figure 8. Contribution of the PB, SE, and ESA components to the calculated kinetics at 77 K upon excitation at 1036 nm and detection at 1010, 1050, 1060, and 1070 nm.

the ESA and PB/SE peaks (near the zero-crossing point) and between the PB and SE regions (in the long-wavelength wing). At these points the amplitude of the oscillations vanishes (see the 1070 nm curve in Figure 7), and the phase is quickly changed by π , i.e., the maxima of the oscillatory pattern at shorter wavelength switch to minima at longer wavelengths with respect to this phase reversal point (see the 1050 and 1080 curves in Figure 7). The situation is different upon excitation near the absorption maximum (Figure 6). In this case there is one phase reversal point, which is close to the zero-crossing point, and in addition there exists a region in the PB/SE component where the phase gradually shifts from 0 to π (instead of jumping by π). The same behavior was obtained for our model three-level system (Figure 3).

For a more detailed analysis we have calculated the contribution of each of the three components (ESA, SE, and PB) to the 1010, 1050, 1060, and 1070 nm kinetics upon 1036 nm excitation (Figure 8). According to this data the phase of the oscillatory part of ESA is always the same (wavelength-independent), with a reversal point near 1025 nm. For example, the oscillatory maximum of the 1010 nm kinetics at 0.6 ps (marked by a vertical bar) turns to minimum which have the same position in the 1050, 1060, and 1070 nm kinetics. The phase of the SE oscillations is also wavelength-independent with a reversal at 1058 nm. Note that there is no relative phase shift (different from π) between the ESA and SE oscillatory patterns. Thus, the SE oscillations at 1070 nm are almost identical to the ESA oscillations at 1010 nm, as well as to the inverted ESA oscillations at 1050–1070 nm. The PB oscillations also have a wavelength-independent phase with a reversal at 1036 nm. But

the relative shift of the PB oscillations with respect to the ESA and SE is about $\pm\pi/2$ (Figure 8). This means that the superposition of these oscillations with their wavelength-dependent amplitudes will result in a wavelength-dependent phase shift. This phenomenon only occurs when the excitation wavelength is in the 1030–1040 nm region, i.e., near the absorption maximum. At 1010 nm the oscillations are determined mostly by the ESA, but there are also weak oscillations in the PB (Figure 8, left top frame). This weak PB contribution gives rise to the small phase shift observed in the ΔA kinetics. At 1050 nm both the ESA and PB oscillations are inverted (with respect to the 1010 nm oscillations). The ΔA oscillations are inverted as well, and they are still determined by the ESA contribution, but slightly shifted due to PB (similar to the 1010 nm oscillations) (Figure 8, left bottom frame). At 1060 nm the PB contribution increases giving rise to an increasing phase shift (Figure 8, right top frame). At longer wavelengths the SE oscillations partially compensate those of the ESA, and the shape of the oscillations is determined mostly by the PB component. The total phase shift of the ΔA oscillations reaches $\pi/2$. At 1070 (Figure 8, right bottom frame) and longer wavelengths the SE component plays a dominant role, inducing a further phase shift from $\pi/2$ to π . Thus, the wavelength-dependent kinetics upon 1036 nm excitation can be unraveled precisely in their various contributions.

Notice that upon 1017 or 1055 nm excitation the oscillatory patterns of the ESA, SE and PB components look similar, but the PB oscillations are now either in-phase or out-of-phase with those of the ESA and SE. This means that the PB contribution does not induce a phase shift but only changes the amplitude

of the total signal and the oscillations show a wavelength-dependent amplitude instead of a wavelength-dependent phase. At the point where the amplitude passes through zero we have a rapid jump of phase. It is also important that for both these excitation wavelengths the oscillations in the red and blue wings of the spectrum are in phase (if we consider the case of the positive displacement of the two-exciton states). In the case of a negative displacement of the two-exciton manifold, we would have had an opposite phase of the ESA component. In that case it would have been impossible to explain the wavelength dependence of the oscillations even at a qualitative level.

Spectral Heterogeneity of the Core Antenna Complexes.

In addition to the oscillations in the time-resolved optical response of LH1 of *Rps. viridis*, there is another consequence of the electron–vibrational coupling, i.e., the fine structure of the linear absorption spectrum due to the presence of vibrational sublevels associated with the electronic (excitonic) levels. This fine structure of exciton levels together with the exciton splitting itself results in very complicated heterogeneous spectra. Typically, the spectral heterogeneity is hidden under the homogeneous and inhomogeneous broadening and can be resolved only at low temperature. Here we discuss the origins of the spectral heterogeneity of the LH1 antenna of *Rps. viridis*⁴⁸ within the framework of our model.

The low-temperature (4 K) absorption band of the LH1 antenna of *Rps. viridis* was found to be heterogeneous.⁴⁸ A Gaussian deconvolution of the absorption spectrum revealed four components at 1044, 1033, 1018, and 984 nm. The corresponding widths (fwhm) are 12.4, 19.8, 32, and 64 nm, respectively. The inverted second derivative of the absorption spectrum (SDA spectrum) showed three maxima at 1049, 1042, and 1030 nm. The first two peaks are very sharp with a width of about 3 and 5 nm, whereas the third is 10 nm broad and has some reproducible substructure. This is in remarkable contrast to the LH1 absorption band of BChl *a* containing species.⁷⁵ For example, the LH1 antennae of *Rb. sphaeroides* at 4 K displays an SDA spectrum corresponding to a single structureless peak.⁷⁶

In our previous paper⁴⁷ we have modeled the linear absorption and pump–probe spectra using a disordered exciton model for the LH1 antenna of *Rps. viridis* (the pigment arrangement was taken to be analogous to that of LH2 of *Rps. acidophila*⁵). The spectral heterogeneity of the LH1 antenna of *Rps. viridis* was explained in terms of the exciton splitting of the major electronic transition due to resonant interactions in a ring-like aggregate of BChls. It was found that the shape of the absorption spectrum is dominated by the five lowest exciton components ($k = 0$, $k = \pm 1$, $k = \pm 2$) which have maxima at 1046–1049, 1039–1042, 1032–1036, 1020–1031, and 1012–1025 nm (depending on parameters of the electronic Hamiltonian). The calculated maxima of the three lowest (most intense) exciton levels are very close to the 1049, 1042, and 1030 nm maxima of the experimental SDA spectrum.⁴⁸ On the other hand, a spectral heterogeneity like this should be a property common to all spectrally disordered circular aggregates. Consequently, the same (or, at least very similar) features may also be expected for the LH1 antennae of the BChl *a*-containing bacteria. However, no heterogeneity was found for these species. We therefore concluded that the possibility to resolve a fine structure in the ensemble spectrum may be strongly dependent on the spectral shapes of individual exciton components. In particular, we proposed that these spectral shapes, which are determined by the exciton–phonon coupling, may be essentially different for the different species.⁴⁷ Here we revisit this problem using our

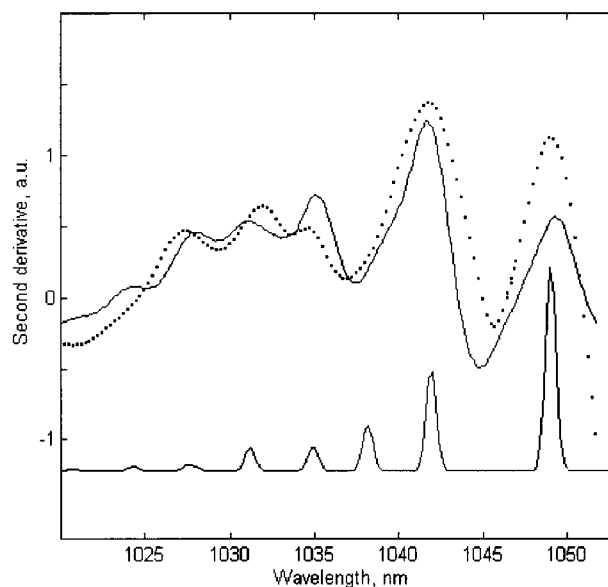


Figure 9. Inverted second derivative of the absorption spectrum (SDA) at 4 K, experiment (points) and calculation (solid lines). The calculated data corresponds to $\Omega_1 = 65 \text{ cm}^{-1}$, $\Omega_2 = 101 \text{ cm}^{-1}$, $S_1 = 0.45$, $S_2 = 0.18$, $\gamma_1 = 7 \text{ cm}^{-1}$, $\gamma_2 = 10 \text{ cm}^{-1}$, $\sigma = 380 \text{ cm}^{-1}$. All other parameters are the same as in Figure 4, but the Γ_{IL} and Λ_{IL} constants were reduced by a factor of 3. The absorption spectrum of the lowest exciton state without inhomogeneous broadening is shown below the SDA spectra (with some shift of the zero level).

exciton–vibrational model in order to further quantify the origins of this spectral heterogeneity.

It should be noticed that our fit of the absorption spectrum at 77 K (Figure 4) is essentially the same as in our previous work.⁴⁷ The positions, widths, and relative intensities of the exciton components are approximately the same, but their shapes are asymmetric due to the presence of vibrational sidebands. The vibrational structure of the single site absorption spectrum is not resolved due to the homogeneous and inhomogeneous broadening of the exciton–vibrational lines and the corresponding SDA spectrum is structureless at 77 K (data not shown). However, this situation changes if we calculate the SDA at 4 K (Figure 9). In this calculation the Γ_{IL} and Λ_{IL} constants were reduced by a factor of 3 to model the increase in the $k = 0$ state lifetime at 4 K. The vibrational frequencies and damping constants are slightly different at 4 and 77 K (see Table 1). The calculated SDA spectrum in Figure 9 corresponds to $\Omega_1 = 65 \text{ cm}^{-1}$, $\Omega_2 = 101 \text{ cm}^{-1}$, $S_1 = 0.45$, $S_2 = 0.18$, $\gamma_1 = 7 \text{ cm}^{-1}$, and $\gamma_2 = 10 \text{ cm}^{-1}$, and the site inhomogeneity $\sigma = 380 \text{ cm}^{-1}$. The thus-calculated spectrum is in good quantitative agreement with the experimental one (Figure 9). For comparison, the absorption profile of the lowest exciton level, $k = 0$, is shown on the same figure (without inhomogeneous broadening). The most intense peaks at 1049 and 1042 nm correspond to the zero-phonon line $\{0,0\}$, and to the first vibronic sublevel of the 65 cm^{-1} mode $\{1,0\}$. The next five peaks at 1038, 1035, 1031, 1028/1027.5, and 1024 nm correspond to the $\{0,1\}$, $\{2,0\}$, $\{1,1\}$, $\{3,0\}/\{0,2\}$, and $\{2,1\}$ vibronic sublevels. The sharp features of the SDA spectrum closely correspond to these vibronic sublevels of the lowest $k = 0$ component, whereas higher exciton levels broadened due to relaxation give rise to broad structureless contribution. The resulting SDA spectrum (Figure 9) has two sharp maxima at 1049 and 1042 nm due to lowest vibronic sublevels of the $k = 0$ state and broad component at 1024–1036 due to higher states $k = \pm 1$ and $k = \pm 2$. The substructure of this broad component is determined by higher vibronic levels of the $k = 0$ state.

The 1044, 1033, and 1018 nm components of the Gaussian deconvolution of the low-temperature absorption correspond to the $k = 0$ level, the $k = \pm 1$ pair, and the $k = \pm 2$ pair of levels (Figure 4), which in our calculation peak at 1050, 1039, and 1023 nm, respectively. The 5–6 nm difference in peak positions originates from the asymmetry of the exciton line shapes.

We conclude that there are two origins for the spectral heterogeneity of LH1: (1) the exciton splitting of the absorption band and (2) the vibrational substructure of the exciton levels. To explain the experimental heterogeneity, for example, the fine structure of the SDA spectra, one should take into account the combined action of these two factors. A narrow and intense peaks in the SDA can only be observed for strong coupling of the excitonic transition to a long-lived (underdamped) vibrational mode as is the case for LH1 of *Rps. viridis*. For other species, for example, for LH1 of *Rb. sphaeroides*, this coupling is significantly weaker and the damping time is about two times less (see Table 1). In this case one should expect weak and broad vibrational lines and, as a result, a structureless SDA spectrum.

Discussion

LH1 Core Antenna of *Rps. viridis*. The BChl *b*-containing bacterium *Rps. viridis* occupies a special position among all the species of purple bacteria. The main absorption band around 1000 nm is very red-shifted and was found to be heterogeneous⁴⁸ in contrast to the LH1 absorption band of the BChl *a* containing species.⁷⁵ The SDA spectrum of the LH1 antennae of *Rps. viridis* at 4 K revealed three clear peaks for *Rps. viridis* while for LH1 of *Rb. sphaeroides* a single peak was obtained.^{75,76} The shape of the low-temperature emission spectrum and the position of the emission maximum (1054 nm) for LH1 of *Rps. viridis* do not change when the excitation wavelength is tuned from the blue to the red edge of the absorption band, i.e., from 1018 to 1047 nm.⁴⁸ In contrast, the emission spectrum of the LH1 complex of *Rb. sphaeroides* is strongly dependent on the excitation wavelength.⁷⁵ The polarization of the emission of the isolated core complexes from *Rps. viridis* starts to increase once the excitation is at longer wavelengths than the maximum of the band,⁴⁸ similarly to isolated core complexes from *Rb. sphaeroides*.⁷⁵ On the other hand, the polarization of the emission of membranes of *Rps. viridis* is constant ($r = 0.1$), and only starts to increase upon excitation in the very red edge (from 1050 nm and redder).⁴⁸ Time-resolved pump–probe measurements of membranes of *Rps. viridis* revealed strong oscillatory features in the kinetics with a surprisingly long decay at all detection wavelengths and all temperatures from 4 to 300 K.²⁹ This is again in contrast with the BChl *a*-containing species where oscillations are weaker and more damped.^{22,24}

The results obtained in this paper suggest that the difference between LH1 from *Rps. viridis* and *Rb. sphaeroides* is connected with a different degree of exciton–phonon coupling. The LH1 antenna of *Rps. viridis* is characterized by a strong coupling to two underdamped low-frequency modes (48–65 and 103–110 cm^{-1}). These modes (or at least the 104–110 cm^{-1} mode) are also present in LH1 of the BChl *a* containing species, but for the latter the coupling to these modes is weaker and moreover their dephasing time is faster. In this paper we have demonstrated that this specific property of *Rps. viridis* is the cause for the strong oscillations in the pump–probe kinetics and for the pronounced heterogeneity of the absorption band due to combined effect of the exciton splitting and vibrational sidebands. It is also important that the homogeneous line shape determined by these vibrational sublevels is very broad (see

Figure 9) and comparable with the inhomogeneous width (which is about $\sigma N^{-1/2}$, i.e., 75–80 cm^{-1} at 4 K). This is in contrast with the LH1 of *Rb. sphaeroides* where the absorption of the lowest level is largely determined by inhomogeneous broadening.⁷⁵ As a result the site-selected emission spectra are strongly dependent on excitation wavelength for *Rb. sphaeroides* but almost wavelength-independent for *Rps. viridis*.

Our model allows us to reproduce the polarization of the emission of the isolated core complexes from *Rps. viridis*⁴⁸ (with a relatively slow increase of the polarization in the red part of the band). We found that this result is only weakly dependent on the ratio between homogeneous and inhomogeneous broadening (data not shown). In particular, a very similar polarization curve can be obtained for the isolated complex with less pronounced vibronic structure, in good agreement with the experimental data for *Rb. sphaeroides*.⁷⁵ To explain the polarization of the emission of membranes of *Rps. viridis*⁴⁸ (constant over the whole band) it is necessary to introduce an excitation transfer between different core complexes. The experimental polarization curve suggests that such a migration must be very effective even upon selective excitation of the red-shifted complexes at low temperature. It is reasonable to suppose that this is a result of enhancement of the spectral overlap between exciton states with pronounced vibronic substructure.

Eigenstate Representation versus Eigenstate-Free Approach. In this paper we used a vibrational eigenstate representation for nonlinear optical response. This approach implies a summation over all possible transitions between exciton–vibrational states, which is practical only for a limited number of vibrational levels. Alternatively, the nonlinear response can be expressed in terms of line broadening functions $g(t)$ which are related to the time correlation function of the electronic energy gap.^{51,77–80} This correlation function reflecting a coupling to nuclear degrees of freedom with an arbitrary spectral density can be evaluated without calculation of vibrational eigenstates. In the case of large number of eigenstates the nuclear dynamics can be calculated semiclassically in terms of wave packets in Liouville space,⁵¹ or in terms of the time-dependent overlap of bra and ket wave packets.^{77–80} The eigenstate-free approach was applied to interpret the vibrational dynamics using multimode harmonic and anharmonic potential surfaces of the excited states.^{77–83} Generalization to the case of an aggregate with many exciton levels was made^{49,61,62} by introducing the matrix of line broadening functions $g_{kk'}(t)$ and $g_{kq}(t)$, where k' , k and q correspond to one- and two-exciton states. The nonlinear response was calculated assuming fast nuclear dephasing as compared with the exciton relaxation/hopping. The opposite limit (corresponding to the case of LH1 antenna) is more difficult to obtain. In principle it can be done using the general expressions of refs 49, 61, and 62 together with a higher-order expansion with respect to the exciton–phonon Hamiltonian.

Long-Lived Vibrational Coherence and Exciton Delocalization. The oscillations observed in the pump–probe kinetics can be used as a test for our model for the exciton dynamics in the antenna. In general, the process of excitation energy transfer involves the coupled dynamics of electronic excitations and collective nuclear motions in the light-harvesting complex. It should be realized that the dynamics of vibrational coherence is closely connected with the exciton dynamics, i.e., with coherent and incoherent motion of the exciton wave packet in the antenna. For example, the decay of the vibrational coherence may be shortened due to incoherent hopping of the exciton wave packet. In its turn, the coupling with vibrations will give rise to

more localized exciton states due to polaron formation. This demonstrates that both vibrational and electronic (excitonic) coherences should be taken into account in the description of the primary processes of energy (and electron) transfer in photosynthesis.

In the model discussed above we have neglected the influence of vibrations on the exciton states, thereby assuming that the polaron length is larger than the disorder-induced localization length. In that case the exciton density matrix becomes independent of the vibrational coordinates and can be obtained from the free-exciton eigenstates. The corresponding density matrixes and related delocalization sizes^{57,72,73} were calculated in a foregoing paper,⁴⁷ where we used the same electronic Hamiltonian as here. We demonstrated that the initially created exciton wave packet relaxes to the steady-state wave packet with a time constant of 130–150 fs. This exciton relaxation is accompanied by the dynamic Stokes shift of the pump–probe spectrum and by the induced anisotropy decay with a very similar time constant. The exciton relaxation does not destroy the vibrational coherence (as can be seen for LH1 of *Rps. viridis*,²⁹ and also for the chlorosomal antenna,⁸⁴ and RCs^{17,21}). In our case the exciton relaxation results in the formation of a steady-state wave packet, which is delocalized over 6–10 BChl molecules at 77K⁴⁷ and coupled to coherent nuclear motion. It seems reasonable to assume that the further migration (noncoherent motion) of the steady-state exciton (polaron) along the circular antenna will induce an additional decay of the vibrational coherences. The time constant of this decay τ_{hop} is connected with the effective time of migration over a distance comparable with the delocalization length. The estimated hopping constant $\tau_{\text{hop}} = 0.9\text{--}1.5$ ps corresponds to a high degree of delocalization. For comparison, if one supposes a fully localized excitation in LH1, then the estimated hopping constant will be less than 100 fs.²⁵

Note, however, that for a correct description of vibrational dephasing via hopping (or, possibly of the transfer of vibrational coherence during the hopping process^{25,29}) a more advanced modeling is needed which explicitly accounts for the interplay between vibrational dynamics and electronic energy transfer. Although a general physical approach to this problem was developed,⁵² all applications of this theory to photosynthetic pigment–proteins were so far restricted to rather simplified models due to the complexity of these systems and due to the lack of information about the structure and the values of the relevant parameters.

Acknowledgment. V.N. was supported by a visitor's grant from the Dutch Foundation of Scientific Research (NWO) and by the Russian Foundation for Basic Research, Grant No. 99-04-49217. The research was supported by the Foundation of Earth and Life Sciences (ALW), part of the Dutch Foundation of Scientific Research, and the Human Frontiers in Science Program, Grant No. 1932802.

References and Notes

- (1) Van Grondelle, R.; Dekker, J. P.; Gillbro, T.; Sundström, V. *Biochim. Biophys. Acta* **1994**, *1187*, 1.
- (2) Fleming, G. R.; van Grondelle, R. *Phys. Today* **1994**, *47*, 48.
- (3) Sundström, V.; Pullerits, T.; van Grondelle, R. *J. Phys. Chem. B* **1999**, *103*, 2327.
- (4) Van Amerongen, H.; Valkunas, L.; van Grondelle, R. *Photosynthetic Excitons*; World Scientific Publishers: Singapore, 2000.
- (5) McDermott, G.; Prince, S. M.; Freer, A. A.; Hawthornthwaite-Lawless, A. M.; Papiz, M. Z.; Cogdell, R. J.; Isaacs, N. W. *Nature* **1995**, *374*, 517.
- (6) Karrasch, S.; Bullough, P. A.; Ghosh, R. *EMBO J.* **1995**, *14*, 631.
- (7) Koepke, J.; Hu, X.; Muenke, C.; Schulten, K.; Michel, H. *Structure* **1996**, *4*, 581.
- (8) Hu, X.; Ritz, T.; Damjanovic, A.; Schulten, K. *J. Phys. Chem. B* **1997**, *101*, 3854.
- (9) Visscher, K. J.; Bergström, H.; Sundström, V.; Hunter, C. N.; van Grondelle, R. *Photosynth. Res.* **1989**, *22*, 211.
- (10) Bergström, H.; van Grondelle, R.; Sundström, V. *FEBS Lett.* **1989**, *250*, 503.
- (11) Beekman, L. M. P.; van Mourik, F.; Jones, M. R.; Visser, H. M.; Hunter, C. N.; van Grondelle, R. *Biochemistry* **1994**, *33*, 3143.
- (12) Martin, J.-L.; Breton, J.; Hoff, A. J.; Migus, A.; Antonetti, A. *Proc. Natl. Acad. Sci. U.S.A.* **1986**, *83*, 957.
- (13) Fleming, G. R.; Martin, J.-L.; Breton, J. *Nature* **1988**, *333*, 190.
- (14) Vos, M. H.; Rappaport, F.; Lambry, J.-Ch.; Breton, J.; Martin, J.-L. *Nature* **1993**, *363*, 320.
- (15) Vos, M.; Jones, M. R.; Hunter, C. N.; Breton, J.; Lambry, J.-Ch.; Martin, J.-L. *Biochemistry* **1994**, *33*, 6750.
- (16) Vos, M.; Jones, M. R.; Hunter, C. N.; Breton, J.; Martin, J.-L. *Proc. Natl. Acad. Sci. U.S.A.* **1994**, *91*, 12701.
- (17) Vos, M.; Breton, J.; Martin, J.-L. *J. Phys. Chem. B* **1997**, *101*, 9820.
- (18) Vos, M.; Jones, M. R.; Martin, J.-L. *Chem. Phys.* **1998**, *233*, 179.
- (19) Streltsov, A. M.; Yakovlev, A. G.; Shkuropatov, A. Ya.; Shuvalov, V. A. *FEBS Lett.* **1996**, *383*, 129.
- (20) Streltsov, A. M.; Vulto, S. I. E.; Shkuropatov, A. Ya.; Hoff, A. J.; Aartsma, T. J.; Shuvalov, V. A. *J. Phys. Chem. B* **1998**, *102*, 7293.
- (21) Arnett, D. C.; Moser, C. C.; Dutton, P. L.; Scherer, N. F. *J. Phys. Chem. B* **1999**, *103*, 2014.
- (22) Chachisvilis, M.; Pullerits, T.; Jones, M. R.; Hunter, C. N.; Sundström, V. *Chem. Phys. Lett.* **1994**, *224*, 345.
- (23) Chachisvilis, M.; Fidler, H.; Pullerits, T.; Sundström, V. *J. Raman Spectrosc.* **1995**, *26*, 513.
- (24) Chachisvilis, M.; Sundström, V. *Chem. Phys. Lett.* **1996**, *261*, 165.
- (25) Bradforth, S. E.; Jimenez, R.; van Mourik, F.; van Grondelle, R.; Fleming, G. R. *J. Phys. Chem.* **1995**, *99*, 16179.
- (26) Joo, T.; Jia, Y.; Yu, J.-Y.; Jonas, D. M.; Fleming, G. R. *J. Phys. Chem.* **1996**, *100*, 2399.
- (27) Jimenez, R.; van Mourik, F.; Yu, J. Y.; Fleming, G. R. *J. Phys. Chem. B* **1997**, *101*, 7350.
- (28) Kumble, R.; Palese, S.; Visschers, R. W.; Dutton, P. L.; Hochstrasser, R. M. *Chem. Phys. Lett.* **1996**, *261*, 396.
- (29) Monshouwer, R.; Baltuska, A.; van Mourik, F.; van Grondelle, R. *J. Phys. Chem. A* **1998**, *102*, 4360.
- (30) Savikhin, S.; Zhu, Y.; Lin, S.; Blankenship, R. E.; Struve, W. S. *J. Phys. Chem.* **1994**, *98*, 10322.
- (31) Savikhin, S.; van Noort, P. I.; Zhu, Y.; Lin, S.; Blankenship, R. E.; Struve, W. S. *Chem. Phys.* **1995**, *194*, 245.
- (32) Agarwal, R.; Krueger, B. P.; Scholes, G. D.; Yang, M.; Yom, J.; Mets, L.; Fleming, G. R. *J. Phys. Chem. B* **2000**, *104*, 2908.
- (33) Zuber, H.; Cogdell, R. J. In *Anoxygenic Photosynthetic Bacteria*; Blankenship, R. E., Madigan, M. T., Bauer, C. E., Eds.; Kluwer Academic Publishers: Dordrecht, 1995; p 315.
- (34) Alden, R. G.; Johnson, E.; Nagarajan, V.; Parson, W. W.; Law, C. J.; Cogdell, R. J. *J. Phys. Chem. B* **1997**, *101*, 4667.
- (35) Scholes, G. D.; Gould, I. R.; Cogdell, R. J.; Fleming, G. R. *J. Phys. Chem. B* **1999**, *103*, 2543.
- (36) Barz, W. P.; Verméglio, A.; Francia, F.; Venturoli, G.; Melandri, B. A.; Oesterheld, D. *1995 Biochemistry* **1995**, *34*, 15248.
- (37) McGlynn, P.; Westerhuis, W. H. J.; Jones, M. R.; Hunter, C. N. *J. Biol. Chem.* **1996**, *271*, 3285.
- (38) Jungas, C.; Ranck, J.-L.; Rigaud, J.-L.; Joliot, P.; Verméglio, A. *EMBO J.* **1999**, *18*, 534.
- (39) Frese, R. N.; Olsen, J. D.; Brannvall, R.; Westerhuis, W. H. J.; Hunter, C. N.; van Grondelle, R. *Proc. Natl. Acad. Sci. U.S.A.* **2000**, *97*, 5197.
- (40) van Mourik, F.; Hawthornthwaite, A. M.; Vonk, C.; Evans, M. B.; Cogdell, R. J.; Sundström, V.; van Grondelle, R. *Biochim. Biophys. Acta* **1992**, *1140*, 85.
- (41) Visser, H. M.; Somsen, O. J. G.; van Mourik, F.; Lin, S.; van Stokkum, I. H. M.; van Grondelle, R. *Biophys. J.* **1995**, *69*, 1083.
- (42) Chachisvilis, M.; Kühn, O.; Pullerits, T.; Sundström, V. *J. Phys. Chem. B* **1997**, *101*, 7275.
- (43) Visschers, R. W.; Chang, M. C.; van Mourik, F.; Parkes-Loach, P. S.; Heller, B. A.; Loach, P. A.; van Grondelle, R. *Biochemistry* **1991**, *30*, 5734.
- (44) van Mourik, F.; van der Oord, J. R.; Visscher, K. J.; Parkes-Loach, P. S.; Loach, P. A.; Visschers, R. W.; van Grondelle, R. *Biochim. Biophys. Acta* **1991**, *1059*, 111.
- (45) Novoderezhkin, V.; Monshouwer, R.; van Grondelle, R. *J. Phys. Chem. B* **1999**, *103*, 10540.
- (46) Savikhin, S.; Struve, W. S. *Biophys. J.* **1994**, *67*, 2002.
- (47) Novoderezhkin, V.; Monshouwer, R.; van Grondelle, R. *Biophys. J.* **1999**, *77*, 666.

- (48) Monshouwer, R.; Visschers, R. W.; van Mourik, F.; Freiberg, A.; van Grondelle, R. *Biochim. Biophys. Acta* **1995**, 1229, 373.
- (49) Meier, T.; Chernyak, V.; Mukamel, S. *J. Chem. Phys.* **1997**, 107, 8759.
- (50) Tanimura, Y.; Mukamel, S. *J. Chem. Phys.* **1994**, 101, 3049.
- (51) Mukamel, S. *Principles of nonlinear optical spectroscopy*; Oxford University Press: New York, 1995.
- (52) Chernyak, V.; Mukamel, S. *J. Chem. Phys.* **1996**, 105, 4565.
- (53) Redfield, A. G. *Adv. Magn. Reson.* **1965**, 1, 1.
- (54) Jean, J. M.; Fleming, G. R. *J. Chem. Phys.* **1995**, 103, 2092.
- (55) Renger, Th.; May, V. *J. Phys. Chem. B* **1997**, 101, 7232.
- (56) Renger, Th.; May, V. *Photochem. Photobiol.* **1997**, 66(5), 618.
- (57) Meier, T.; Zhao, Y.; Chernyak, V.; Mukamel, S. *J. Chem. Phys.* **1997**, 107, 3876.
- (58) Zhao, Y.; Brown, D. W.; Lindenberg, K. *J. Chem. Phys.* **1997**, 107, 3159.
- (59) Brown, D. W.; Lindenberg, K.; Zhao, Y. *J. Chem. Phys.* **1997**, 107, 3179.
- (60) Davydov, A. S. *Theory of molecular excitons*; Plenum Press: New York, 1971.
- (61) Zhang, W. M.; Meier, T.; Chernyak, V.; Mukamel, S. *J. Chem. Phys.* **1998**, 108, 7763.
- (62) Zhang, W. M.; Meier, T.; Chernyak, V.; Mukamel, S. *Philos. Trans. R. Soc. London A* **1998**, 356, 405.
- (63) Förster, T. In *Modern Quantum Chemistry*; Academic Press: New York, 1965; Vol. III, p 93.
- (64) Yan, Y. J.; Fried, L. E.; Mukamel, S. *J. Phys. Chem.* **1989**, 93, 8149.
- (65) Yan, Y. J.; Mukamel, S. *Phys. Rev. A* **1990**, 41, 6485.
- (66) Leegwater, J. A. *J. Phys. Chem.* **1995**, 99, 11605.
- (67) Miller, K. R. *Nature* **1982**, 300, 53.
- (68) Stark, W.; Kuhlbrandt, W.; Wildhaber, I.; Wehrli, E.; Muhlethaler, K. *EMBO J.* **1984**, 3, 777.
- (69) Zuber, H.; Brunisholz, R. A. In *The Chlorophylls*; Scheer, H., Ed.; CRC Press: Boca Raton, FL, 1991; p 627.
- (70) Walz, T.; Jamieson, S. J.; Bowers, C. M.; Bullough, P. A.; Hunter, C. N. *J. Mol. Biol.* **1998**, 282, 833.
- (71) Ikedayamasaki, I.; Odahara, T.; Mitsuoaka, K.; Fujiyoshi, Y.; Murata, K. *FEBS Lett.* **1998**, 425, 505.
- (72) Meier, T.; Chernyak, V.; Mukamel, S. *J. Phys. Chem. B* **1997**, 101, 7332.
- (73) Kühn, O.; Sundström, V. *J. Chem. Phys.* **1997**, 107, 4154.
- (74) Monshouwer, R.; Abrahamsson, M.; van Mourik, F.; van Grondelle, R. *J. Phys. Chem. B* **1997**, 101, 7241.
- (75) van Mourik, F.; Visschers, R. W.; van Grondelle, R. *Chem. Phys. Lett.* **1992**, 193, 1.
- (76) Wendling, M. Personal communication.
- (77) Pollard, W. T.; Fragnito, H. L.; Bigot, J.-Y.; Shank, C. V.; Mathies, R. A. *Chem. Phys. Lett.* **1990**, 168, 239.
- (78) Pollard, W. T.; Lee, S.-Y.; Mathies, R. A. *J. Chem. Phys.* **1990**, 92, 4012.
- (79) Pollard, W. T.; Mathies, R. A. *Annu. Rev. Phys. Chem.* **1992**, 43, 497.
- (80) Pollard, W. T.; Dexheimer, S. L.; Wang, Q.; Peteanu, L. A.; Shank, C. V.; Mathies, R. A. *J. Phys. Chem.* **1992**, 96, 6147.
- (81) Yang, T. S.; Chang, M.-S.; Chang, R.; Hayashi, M.; Lin, S. H.; Vöhringer, P.; Dietz, W.; Scherer, N. F. *J. Chem. Phys.* **1999**, 110, 12070.
- (82) de Boeij, W. P.; Pshenichnikov, M. S.; Wiersma, D. A. *J. Phys. Chem.* **1996**, 100, 11806.
- (83) Joo, T.; Jia, Y.; Yu, J.-Y.; Lang, M. J.; Fleming, G. R. *J. Chem. Phys.* **1996**, 104, 6089.
- (84) Cherepy, N. J.; Du, M.; Holzwarth, A. R.; Mathies, R. A. *J. Phys. Chem.* **1996**, 100, 4662.